Kirk-Othmer Encyclopedia of Chemical Technology.

LIGHT EMITTING DIODES

1. Introduction

During the past 40 years, light-emitting diodes (LEDs) have undergone a significant evolution. The first LED emitting in the visible wavelength region was based on GaPAs compound semiconductors and it had an external efficiency $< 1.0\%$. Today, the external efficiencies of red LEDs based on AlGaInP can $>50\%$ and this semiconductor is also capable of emitting at orange, amber, and yellow wavelengths, albeit with lower efficiency. The AlGaInN compounds can emit efficiently in the near ultraviolet (uv), violet, blue, cyan, and green wavelength range. Thus, all colors of the visible spectrum are now covered by semiconductor materials. This opens the possibility to use LEDs in areas beyond conventional indicator and signage applications. In particular, as device output powers steadily increase, LED packages are expected to reach luminous flux levels comparable to those of incandescent and fluorescent sources. Furthermore, LED lifetimes exceeding 10^4 h compare very favorably with incandescent sources ($\sim$500 h) and fluorescent sources ($\sim$5000 h), thereby contributing to the attractiveness of LEDs.

Inorganic LEDs are generally based on p–n junctions. However, in order to achieve high internal quantum efficiencies, free carriers need to be spatially confined. Furthermore, to reduce reabsorption effects, the energy gap of the confinement layers should be higher than the energy gap of the active region. These requirements led to the development of heterostructure LEDs that employ different semiconductor materials or alloy compositions for the light-emitting active region and the confinement regions. Particularly popular are multiple quantum wells embedded into the active region. The light-extraction efficiency, which measures the fraction of photons leaving the semiconductor die (and thus become useful, ie, visible photons), is strongly affected by the device shape and surface structure. For devices with high internal efficiency, the maximization of the light-extraction efficiency is a key challenge.

This article reviews important aspects of inorganic LED structures. The section Basic Properties of High-Emitting Devices introduces the basic concepts of optical emission. Band diagrams of direct- and indirect-gap semiconductors and the spectral shape of spontaneous emission will be discussed along with electrical properties and current flow. The section Device Efficiencies discusses internal and external device efficiencies and strategies to increase them. Spontaneous emission can be enhanced by placing the active region inside an optical resonator, which results in a substantial modification of the LED emission characteristics. The theory and experimental results of such resonant-cavity LEDs (RCLEDs) are discussed in the section Resonant-Cavity enhanced structures. Due to total internal reflection at the surfaces of an LED die (a "die" is a semiconductor chip), the light-extraction efficiency in standard devices is well below 100%. A particular challenge in achieving efficient emission is the minimization of optical absorption processes inside the semiconductor. This can be achieved by covering absorbing regions, such as absorbing substrates, with highly reflective mirrors. Such mirrors should have omnidirectional reflection characteristics and a high angle-integrated, transversal electric-transversal magentic (TE–TM) averaged reflectivity. Electrically conductive omnidirectional reflectors are discussed in the section Omni-Directional Reflectors. In the section White LEDs, several approaches to white

2 LIGHT EMITTING DIODES

LEDs, including phosphor-based approaches and multiple-LED approaches, are presented and their properties, such as color rendering, luminous efficiency and efficacy, are discussed. The section Packaging reviews the current state of the art in LED packaging including packages with low thermal resistance.

2. Basic Properties of Light-Emitting Diodes

2.1. Optical Emission Spectra

The physical mechanism by which semiconductor LEDs emit light is spontaneous recombination of an electron–hole pair and simultaneous emission of a photon. The spontaneous emission process is fundamentally different from the stimulated emission process occurring in semiconductor lasers and superluminescent LEDs. The characteristics of spontaneous emission that determine the optical properties of LEDs will be discussed in this section.

The probability that electrons and holes recombine radiatively is proportional to the electron and hole concentrations, ie, $R \propto n\mathrm{p}$. The recombination rate per unit time per unit volume can be written as

$$R = -\frac{\mathrm{d}n}{\mathrm{d}t} = -\frac{\mathrm{d}p}{\mathrm{d}t} = B\,\mathrm{n}\,\mathrm{p} \tag{1}$$

where B is the *bimolecular recombination coefficient*, with a typical value of 10^{-10} cm^3/s for direct-gap III–V semiconductors.

Electron–hole recombination is illustrated in Fig. 1. Electrons in the conduction band and holes in the valence band are assumed to have the parabolic dispersion relations

$$E = E_{\mathrm{C}} + \frac{\hbar^2 k^2}{2\,m_{\mathrm{e}}^*} \quad \text{(for electrons)} \tag{2}$$

and

$$E = E_{\mathrm{V}} + \frac{\hbar^2 k^2}{2\,m_{\mathrm{h}}^*} \quad \text{(for holes)} \tag{3}$$

where $m_{\mathrm{e}}{}^*$ and $m_{\mathrm{h}}{}^*$ are the electron and hole effective masses, $\hbar$ is Planck's constant divided by 2π, k is the carrier wavenumber, and E_{V} and E_{C} is the valence and conduction band-edge energy, respectively.

The requirement of energy and momentum conservation leads to further insight into the radiative recombination mechanism. It follows from the Boltzmann distribution that electrons and holes have an average kinetic energy of kT. Energy conservation requires that the photon energy is given by the difference between the electron energy, E_{e}, and the hole energy, E_{h}, ie,

$$h\,\nu = E_{\mathrm{e}} - E_{\mathrm{h}} \approx E_{\mathrm{g}} \tag{4}$$

The photon energy is approximately equal to the bandgap energy, E_{g}, if the thermal energy is small compared with the bandgap energy, ie, $kT \ll E_{\mathrm{g}}$. Thus the desired emission wavelength of an LED can be attained by choosing a semiconductor material with appropriate bandgap energy. For example, GaAs has a bandgap energy of 1.42 eV at room temperature resulting in infrared (ir) emission at a wavelength of 870 nm.

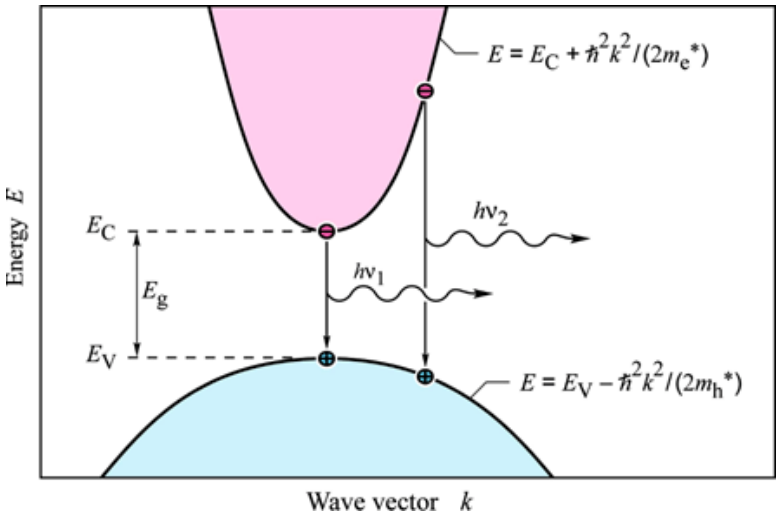

Fig. 1. Parabolic electron and hole dispersion relations showing "vertical" electron–hole recombination and photon emission.

It is helpful to compare the average carrier momentum with the photon momentum. A carrier with kinetic energy kT and effective mass m^* has the momentum

$$p = m^* v = \sqrt{2\, m^* 0.5 m^* v^2} = \sqrt{2\, m^* kT} \tag{5}$$

The momentum of a photon with energy E_g can be obtained from the de Broglie relation

$$p = \hbar k = h\nu/c = E_g/c \tag{6}$$

Calculation of the carrier momentum (using eq. 5) and the photon momentum (using eq. 6) yields that the carrier momentum is *orders of magnitude larger* than the photon momentum. Therefore, the electron momentum must not change during the transition. The transitions are therefore "vertical" as shown in Fig. 1, ie, electrons recombine with only those holes that have the same momentum or k value.

By using the requirement that electron and hole momenta are the same, the photon energy can be written as the *joint dispersion relation*

$$h\nu = E_C + \frac{\hbar^2 k^2}{2\, m_e^*} - E_V + \frac{\hbar^2 k^2}{2\, m_h^*} = E_g + \frac{\hbar^2 k^2}{2\, m_r^*} \tag{7}$$

where m_r^* is the reduced mass given by

$$\frac{1}{m_r^*} = \frac{1}{m_e^*} + \frac{1}{m_h^*} \tag{8}$$

By using the joint dispersion relation, the joint density of states can be calculated and one obtains

$$\rho(E) = \frac{1}{2\pi^2}\left(\frac{2m_r^*}{\hbar^2}\right)^{3/2}\sqrt{E - E_g} \tag{9}$$

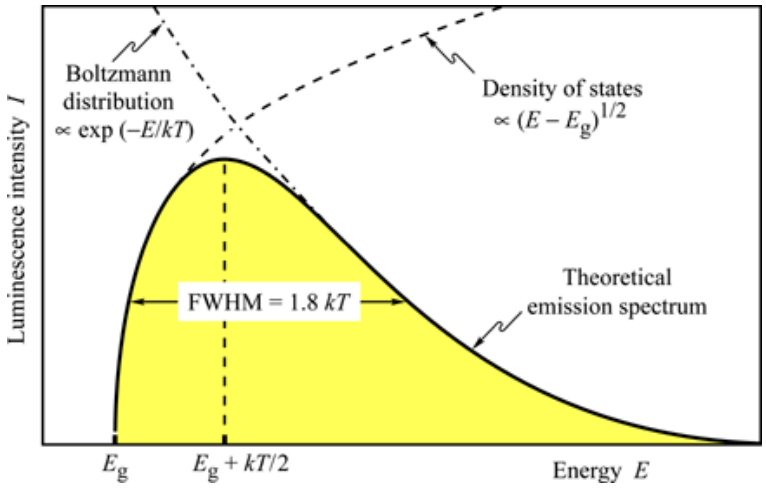

Fig. 2. Theoretical emission spectrum of an LED. The full width at half-maximum (fwhm) of the emission line is 1.8 kT.

The distribution of carriers in the allowed bands is given by the Boltzmann distribution, ie,

$$f_{\mathrm{B}}(E) = \mathrm{e}^{-E/(k\,T)} \tag{10}$$

The *emission intensity* as a function of energy is proportional to the product of equations (9) and (10), ie,

$$I(E) \propto \sqrt{E - E_{\mathrm{g}}}\,\mathrm{e}^{-E/(kT)} \tag{11}$$

The emission line shape of an LED, as given by equation 11, is shown in Fig. 2. The maximum emission intensity occurs at

$$E = E_{\mathrm{g}} + \frac{1}{2} k\,T \tag{12}$$

The full width at half-maximum (fwhm) of the emission is given by

$$\Delta E = 1.8 k\,T \tag{13}$$

For example, the theoretical room temperature linewidth of a GaAs LED emitting at 870 nm is

$$\Delta E = 46\ \mathrm{meV} \text{ or } \Delta\lambda = 28\ \mathrm{nm}.$$

The spectral line width of LED emission is important in several respects. *First*, the line width of an LED emitting in the visible range is relatively narrow compared with the range of the entire visible spectrum. Furthermore, the LED emission is narrower than the spectral width of a single color. For example, *red* colors range from 625 to 730 nm ($\Delta\lambda = 105$ nm), which is much wider than the typical emission spectrum of a red LED ($\Delta\lambda \approx 25$ nm). Therefore, LED emission is perceived by the human eye as monochromatic. *Second*, optical fibers are dispersive, which leads to a range of propagation velocities for a light pulse comprising a range of wavelengths. The material dispersion in optical fibers limits the "*bit rate* × *distance product*" achievable with

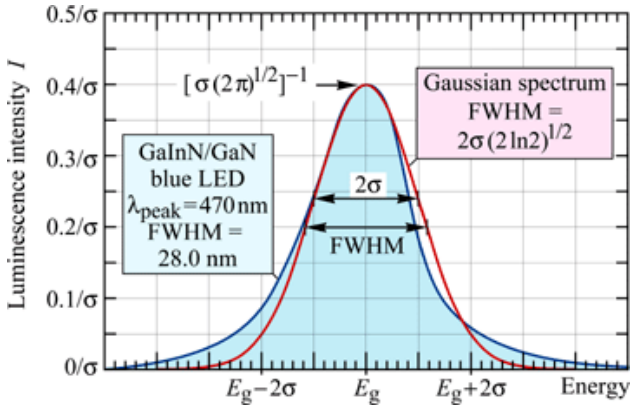

Fig. 3. Theoretical emission spectrum of a semiconductor exhibiting substantial alloy broadening. The fwhm is related to the standard deviation (σ) by the equation shown in the figure.

LEDs. The spontaneous lifetime of carriers in LEDs in direct-gap semiconductors typically is of the order of 1–100 ns depending on the active region doping concentration (or carrier concentrations) and the material quality. Thus, modulation speeds up to 1 Gbit/s are attainable with LEDs.

A spectral width of 1.8 kT is expected for the thermally broadened emission. However, due to other broadening mechanisms, such as *alloy broadening* (ie, the statistical fluctuation of the active region alloy composition), the spectral width at room temperature in III–V nitride LEDs can be broader, typically 3 kT–8 kT. Experimental evidence shown in Fig. 3 supports the use of a Gaussian function to describe the spectral power density function of an LED. Therefore,

$$P(\lambda) = P\frac{1}{\sigma\sqrt{2\pi}}\exp\left[-\frac{1}{2}\left(\frac{\lambda-\lambda_{\text{peak}}}{\sigma}\right)^2\right] \tag{14}$$

where P is the total optical power emitted by the LED. Inspection of Fig. 3 reveals that the Gaussian curve is indeed a very good match for the experimental emission spectrum. Giving the line widths in terms of units of kT is very useful as it allows for convenient comparison of experimental line widths with the theoretical line width of 1.8 kT.

The emission spectra of an AlGaInP red, GaInN green, GaInN blue, GaInN UV, and AlGaN deep uv LEDs are shown in Fig. 4. The LEDs shown in Fig. 4 have an active region comprised of a ternary or quaternary alloy, eg, $Ga_{1-x}In_xN$. In this case, alloy broadening leads to spectral broadening that goes beyond 1.8 kT. Alloy broadening due to inhomogeneous distribution of In in the active region of green $Ga_{1-x}In_xN$ LEDs can cause linewidths as wide as 10 kT at room temperature (1). Note, however, that a recent study found inhomogeneous strain distribution in GaInN quantum wells as a result of electron damage during transmission electron microscopy (TEM) experiments (2). It was concluded that the damage might lead to a "false" detection of In-rich clusters in a homogeneous quantum well structure.

Efficient radiative recombination occurs in direct-gap semiconductors. The recombination probability is much lower in indirect-gap semiconductors because a phonon is required to satisfy momentum conservation. The radiative efficiency of indirect-gap semiconductors can be increased by isoelectronic impurities, eg, N in GaP. Isoelectronic impurities form an optically active deep level that is localized in real space (small Δx) but, as a result of the uncertainty relation, delocalized in k space (large Δk), so that recombination via the impurity satisfies momentum conservation.

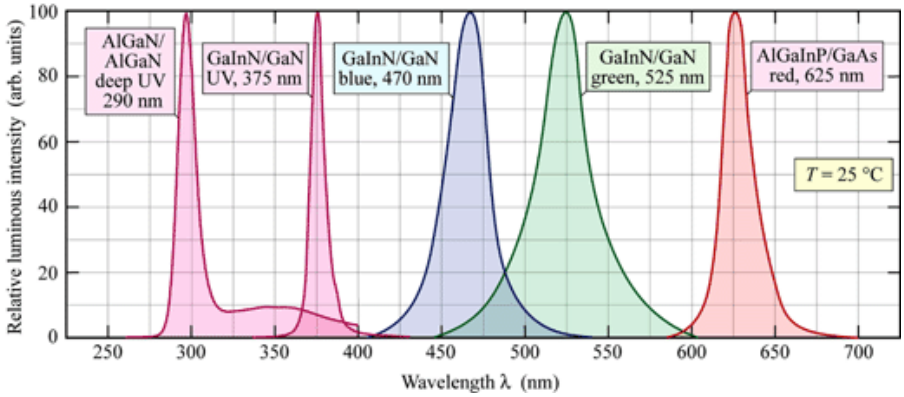

Fig. 4. Emission spectrum of AlGaInP/GaAs red, GaInN/GaN green, GaInN/GaN blue, GaInN/GaN uv, and AlGaN/AlGaN deep uv LEDs at room temperature. (Adopted from Refs. 3,4,5).

During *nonradiative* recombination, the electron energy is converted to vibrational energy of lattice atoms, ie, phonons. There are several physical mechanisms by which nonradiative recombination can occur with the most common ones being recombination at point defects (impurities, vacancies, interstitials, antisite defects, and impurity complexes) and at spatially extended defects (screw and edge dislocations, cluster defects). The defects act as efficient recombination centers (Shockley-Read recombination centers) in particular, if the energy level is close to the middle of the gap.

2.2. Electrical Properties

In the vicinity of the unbiased p–n junction plane shown in Fig. 5**a**, electrons originating from donors on the n-type side diffuse to the p-type side where they recombine. A corresponding process occurs with holes. As a result, a region near the p–n junction, the *depletion region*, is depleted of free carriers. In the absence of free carriers, the types of charges in the depletion region are ionized donor and acceptor charges. The depletion region produces a potential, the *diffusion voltage*, V_{D}, given by

$$V_{\mathrm{D}}=\frac{kT}{e}\ln\frac{N_{\mathrm{A}}N_{\mathrm{D}}}{n_i^2} \tag{15}$$

where N_{A} and N_{D} is the acceptor and donor concentration, respectively, and n_{i} is the intrinsic carrier concentration of the semiconductor. The diffusion voltage represents a barrier that free carriers must overcome in order to reach the neutral region of opposite conductivity type.

The width of the depletion region is given by

$$W_D=\sqrt{\frac{2\,\epsilon}{e}(V_D-V)(\frac{1}{N_A}+\frac{1}{N_D})} \tag{16}$$

where $\epsilon=\epsilon_{\mathrm{r}}\,\epsilon_0$ is the dielectric permittivity of the semiconductor and V is the diode bias voltage.

An external bias applied to a p–n junction will drop across the depletion region, which is resistive due to the lack of free carriers. A forward bias decreases the p–n junction barrier causing electrons and holes to be injected into the neutral regions with opposite conductivity type. As the current increases, carriers diffuse into the regions of opposite conductivity type and recombine, thereby emitting photons.

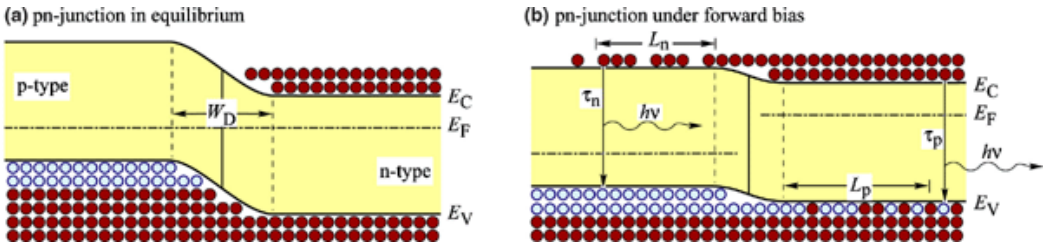

Fig. 5. Band diagram and carrier distribution of a p–n homojunction (**a**) without and (**b**) with applied forward bias. $L_{n/p}$ and $\tau_{n/p}$ are the minority carrier diffusion lengths and lifetimes, respectively. The parameter W_D is the width of the depleted region.

The theory of current transport in p–n junctions was first developed by William Shockley in the early 1950s and the equation describing the I–V characteristic is known as the *Shockley equation*

$$I = eA\left(\sqrt{\frac{D_p}{\tau_p}}\,\frac{n_i^2}{N_D} + \sqrt{\frac{D_n}{\tau_n}}\,\frac{n_i^2}{N_A}\right)\left(e^{eV/kT} - 1\right) \tag{17}$$

where A is the junction area and $D_{n,p}$ and $\tau_{n,p}$ are the electron and hole diffusion constants and minority carrier lifetimes, respectively.

Under typical forward bias conditions, the diode voltage is $V \gg kT/e$, and thus $[\exp(eV/kT) - 1] \approx \exp(eV/kT)$. For such forward bias conditions, the Shockley equation can be rewritten as

$$I = e\,A\left(\sqrt{\frac{D_p}{\tau_p}}\,NA + \sqrt{\frac{D_n}{\tau_n}}\,N_D\right)e^{e(V - V_D)/kT} \tag{18}$$

The exponent in equation (18) illustrates that the current strongly increases as the diode voltage approaches a *threshold*, which is about equal to the diffusion voltage, ie, $V_{th} \approx V_D$.

In an ideal diode, every electron injected into the active region will generate a photon. Thus conservation of energy requires that the electron energy eV equals the photon energy $h\nu$, ie,

$$eV = h\nu \tag{19}$$

Beyond turn-on, the diode becomes highly conductive and the diode voltage V is about the same as the threshold voltage V_{th}. The energy of photons emitted from a semiconductor with energy gap E_g is given by

$$h\nu = E_g + (0.5)kT \approx E_g \tag{20}$$

Thus equation (19) can be rewritten as

$$V_{th} \approx V_D \approx E_g/e \tag{21}$$

Diode I–V characteristics of AlGaInP red and GaInN green and blue LEDs are shown in Fig. 6. The experimental threshold voltages shown in the figure and the comparison with the bandgap energy of these materials indicate that the energy gap and the threshold voltage indeed agree reasonably well.

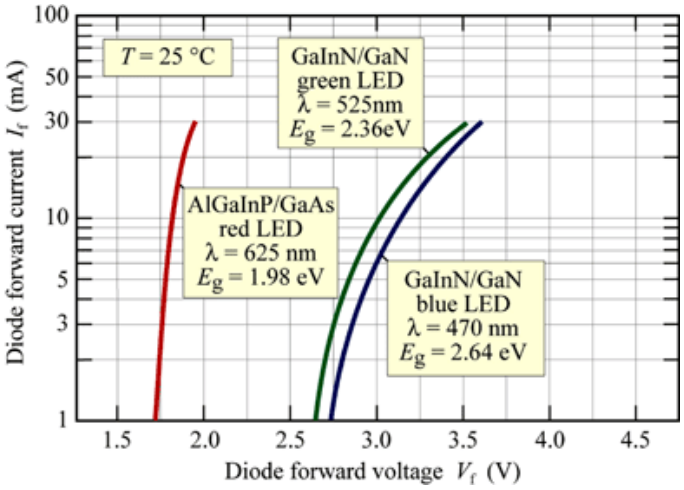

Fig. 6. Forward current–voltage characteristic of GaInN/GaN blue, GaInN/GaN green, and AlGaInP/GaAs red LEDs.

2.3. Current Transport in LED Structures

The LEDs can be grown on conductive as well as insulating substrates. Whereas the current flow is mostly vertical (normal to the substrate plane) in structures grown on conductive substrates, it is mostly lateral (horizontal) in devices grown on insulating substrates. The location and size of ohmic contacts are relevant to light extraction, as metal contacts generally are opaque. This section discusses the current flow patterns of different device structures aimed at high extraction efficiency.

In LEDs with thin top confinement layers, the current is injected into the active region mostly under the top electrode. Thus, light is generated under an opaque metal electrode, which results in a low extraction efficiency. The problem can be avoided with a *current-spreading layer* or *window layer* that spreads the current under the top electrode to regions not covered by the opaque top electrode.

The usefulness of current-spreading layers was shown by Nuese and co-workers (6) who demonstrated a substantial improvement of the optical output power in GaAsP LEDs. The effect of the current-spreading layer is illustrated schematically in Fig. 7**a**. Current-spreading layers are employed in top-emitting LEDs. A GaP current-spreading layer in an AlGaInP LED was reported by Kuo and co-workers (7) and Fletcher and co-workers (8,9). The AlGaAs current spreading layers in AlGaInP LEDs were reported by Sugawara and co-workers (10,11,12).

For circular contact geometry, the thickness of the current spreading layer, t, results a current spreading length L_s given by equation 22 (13)

$$t = \rho\, L_s (r_c + \frac{L_s}{2}) \ln(1 + \frac{L_s}{r_c}) (J_0 \frac{e}{n_{ideal}\, kT}) \tag{22}$$

where J_0 is the current density at the edge of the contact, r_c is the contact radius. The equation allows one to calculate the required current-spreading layer thickness t for a given resistivity of this layer and the desired current spreading length L_s.

Current crowding also occurs in mesa-structure LEDs grown on *insulating* substrates, eg, GaInN/GaN LEDs grown on sapphire substrates. In common GaInN devices, the p-type contact is located on the top of the mesa, and the n-type contact is located on an n-type buffer layer at the bottom of the mesa. As a result, the current crowds at the edge of the mesa contact adjoining the n-type contact.

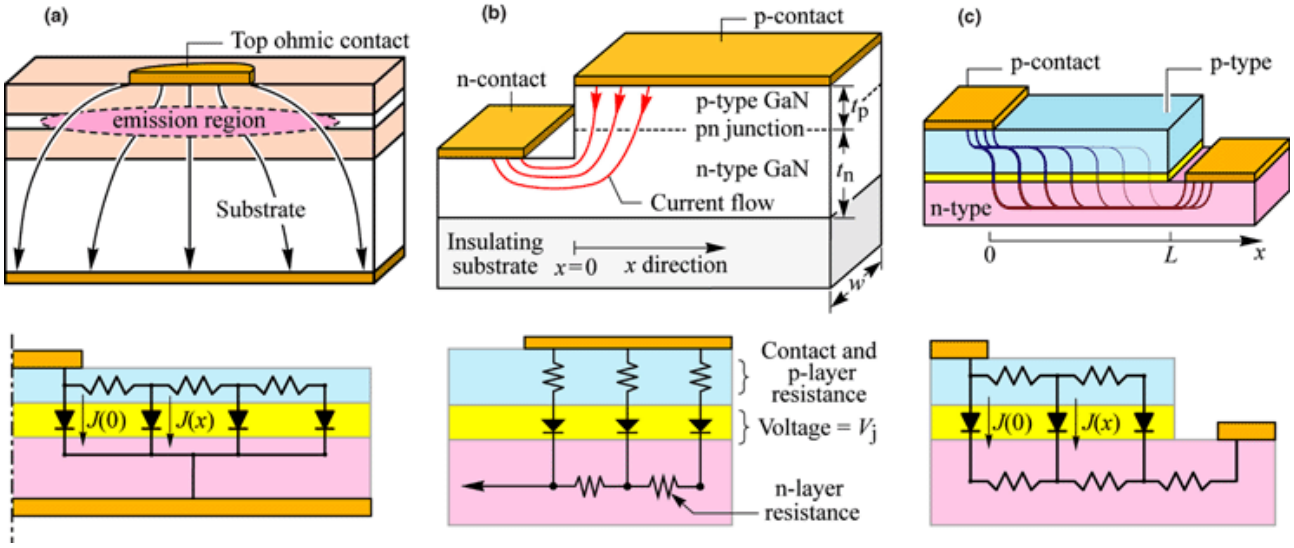

Fig. 7. (**a**) Current-spreading structure used in AlGaInP LEDs. (**b**) Current crowding in a mesa-structure GaN-based LED grown on an insulating substrate. (**c**) Lateral injection geometry. The corresponding equivalent circuits are shown as well.

A lateral p-side-up mesa LED grown on an insulating substrate is shown in Fig. 7**b**. It is intuitively clear that the p–n junction current crowds near the edge of the mesa as indicated in the figure. An equivalent circuit model is shown in Fig. 7**b** and includes the p-type contact resistance and the resistances of the n- and p-type cladding layers. The p–n junction is approximated by an ideal diode. The circuit model also shows several nodes separated by a distance dx. The current distribution decreases exponentially with distance from the contact edge. The current spreading length is given by equation 23 (14)

$$L_s = \sqrt{(\rho_c + \rho_p t_p) t_n / \rho_n} \tag{23}$$

where $\rho_{n,p}$ and $t_{n,p}$ are the resistivities and thickness of the n- and p-type layers, respectively, and ρ_c is the specific contact resistance. The equation shows that the current distribution depends on epitaxial layer thicknesses and material resistivities. A thick low resistivity n-type buffer layer is needed to ensure that current crowding is minimized. For *low* p-type contact and confinement resistances, strong current crowding results, unless the n-type buffer layer is very conductive so that t_n/ρ_n is very large. In GaN/GaInN devices, the sum of p-type contact and p-type layer resistances can be larger than the n-type cladding resistance, especially if t_n is small.

A device structure with a lateral current-injection scheme is shown in Fig. 7**c**. The current is transported laterally in both the n- and p-type cladding layers. Light is generated in the region between the contacts, where the extraction is not hindered by contacts. If the n-type sheet resistance ρ_n/t_n is much lower than the p-type sheet resistance ρ_p/t_p, the current prefers to flow laterally in the low resistance n- rather than the p-layer. As a result, the junction current crowds near the p-type contact. A schematic equivalent circuit suitable for the quantitative analysis is shown in Fig. 7**c** where a p–n junction current density of $J(0)$ is assumed at the edge of the p-type contact. The analytic solution of the equivalent circuit shown in Fig. 7**c** is an exponential function (15,16).

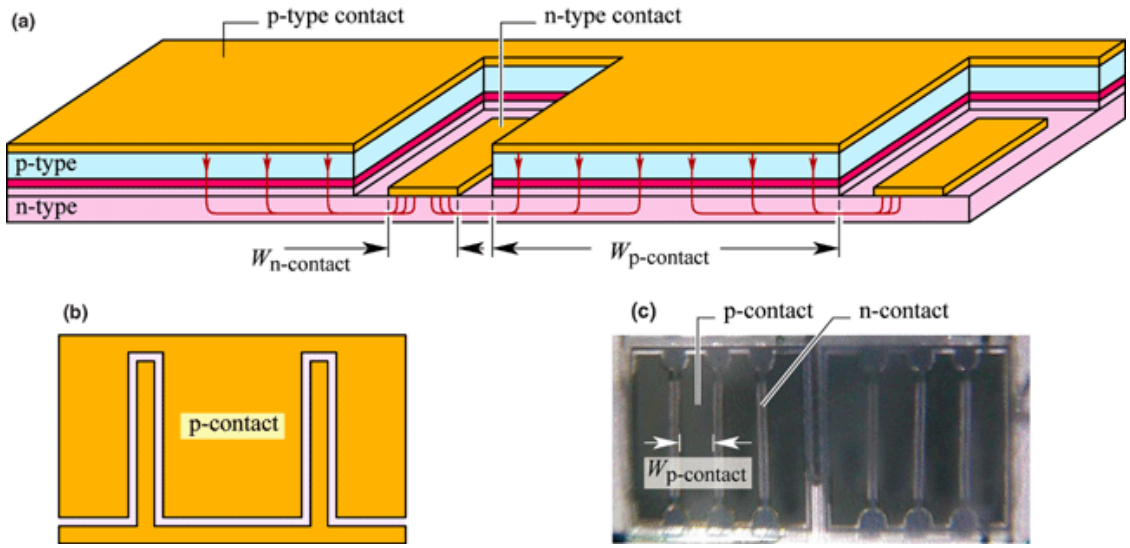

Fig. 8. (**a**) Interdigitated stripe-contact structure for uniform current injection. (**b**) Top view. (**c**) Photograph of flip-chip GaInN LED. (Adopted from LED Museum, see Ref. 17.)

For uniform light generation across the gap between the contacts, it is desirable to have a long exponential decay length L_s. This can be achieved by high doping or thick confinement layers. To attain high powers, one may be tempted to scale the device structure in size. However, for large contact separations L, the device becomes generally more resistive unless very thick confinement layers are being used, which may be unpractical. Scaling such device structures can be accomplished by employing arrays of many small devices rather than scaling up a single device.

Note that current crowding becomes increasingly severe with larger device sizes, unless novel contact geometries are introduced to alleviate the problem. Such novel contact geometries include interdigitated structures with p-type finger widths $< L_s$ (18,19). For device dimensions much smaller than L_s, the current crowding effect can be neglected.

The schematic structure and a photograph of an interdigitated stripe-contact geometry are shown in Fig. 8. Uniform current injection into the active region is achieved by the p-type contact width ($W_{\text{p-contact}}$) being smaller than the current spreading length. The width of the n-type contact ($W_{\text{n-contact}}$) must be at least equal to the contact transfer length to ensure low contact resistance. The contact transfer length follows from the transmission line model (TLM) used for characterization of ohmic contacts (20).

3. Device Efficiencies

The *internal quantum efficiency* of a current-injected semiconductor device is given by

$$\eta_{\text{int}} = \frac{\text{number of photons emitted from active region per second}}{\text{number of electrons injected into LED per second}} = \frac{P_{\text{int}}/(h\,\nu)}{I/e} \tag{24}$$

where P_{int} is the optical power emitted from the active region and I is the injection current. Not all photons emitted by the active region will escape from the semiconductor die. The light *extraction efficiency* is defined as

$$\eta_{\text{extraction}} = \frac{\text{number of photons emitted into free space per second}}{\text{number of photons emitted from active region per second}} = \frac{P/(h\,\nu)}{P_{\text{int}}/(h\,\nu)} \tag{25}$$

where P is the optical power emitted into free space.

The *external quantum efficiency* is defined as

$$\eta_{\text{ext}} = \frac{\text{number of photons emitted into free space per second}}{\text{number of electrons injected into LED per second}} = \frac{P/(h\,\nu)}{I/e} = \eta_{\text{int}}\,\eta_{\text{extraction}} \tag{26}$$

The external quantum efficiency gives the ratio of the number of useful light particles to the number of injected charge particles.

The *power efficiency* is defined as

$$\eta_{\text{power}} = P/(I\,V) \tag{27}$$

where IV is the electrical power provided to the LED. Informally, the power efficiency is also called "*wall-plug efficiency*".

For visible-spectrum LEDs, the *luminous efficacy of radiation* is defined as the luminous flux emitted by the source divided by the optical power, ie,

$$\eta_{\text{lum radiation}} = 683\frac{\text{lm}}{\text{W}}\int_{\lambda} V(\lambda)\,P(\lambda)\,\mathrm{d}\lambda \Big/ \int_{\lambda} P(\lambda)\,\mathrm{d}\lambda \tag{28}$$

where 683 lm/W is a normalization factor and $V(\lambda)$ is the eye sensitivity function. The *luminous efficiency of the source* is defined as the luminous flux emitted by the source divided by the input electrical power, ie,

$$\eta_{\text{lum source}} = 683\frac{\text{lm}}{\text{W}}\int_{\lambda} V(\lambda)\,P(\lambda)\,\mathrm{d}\lambda/(I\,V) \tag{29}$$

where IV is the LED input electrical power.

3.1. High Internal-Efficiency Structures

The radiative recombination rate R is proportional to the product of the carrier concentrations n and p. Therefore high concentration of carriers in the active region decreases the radiative carrier lifetime and the probability of nonradiative recombination.

The distribution of carriers in a p–n *homojunction* was shown in Fig. 5. The minority carrier concentration decreases exponentially with distance from the p–n junction. The mean distance that a minority carrier diffuses before recombination is the *diffusion length* $L_{\text{n/p}}$, which is given by

$$L_{\text{n}} = \sqrt{D_{\text{n}}\,\tau_{\text{n}}} \;\text{ and }\; L_{\text{p}} = \sqrt{D_{\text{p}}\,\tau_{\text{p}}} \tag{30}$$

where τ_{n} and τ_{p} are the electron and hole minority carrier lifetimes, respectively. In typical semiconductors, the diffusion length is of the order of micrometers. For example, the diffusion length of electrons in p-type GaAs

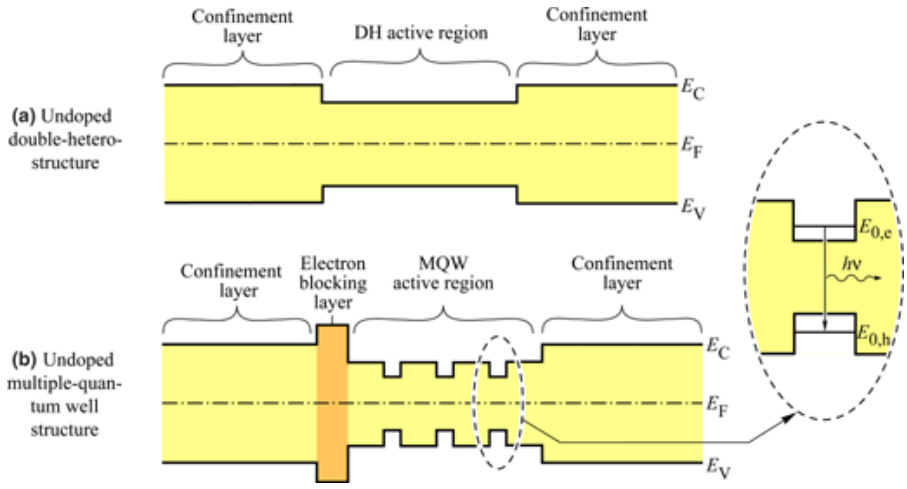

Fig. 9. Band diagrams of undoped (**a**) DH and (**b**) MQW structures. The MQW structure employs an electron-blocking layer to avoid electron leakage out of the MQW active region. The inset shows the quantum well region and optical transition between quantized states.

is $L_n = (220\ \text{cm}^2/\text{s} \times 10^{-8}\ \text{s})^{1/2} = 15\ \mu\text{m}$. Thus, minority carriers are distributed over a region several microns thick and recombination occurs within a relatively large volume.

All high brightness LEDs employ *heterostructures* or *quantum wells*. A structure consisting of two barriers, ie, two large-bandgap semiconductors, is a *double heterostructure* (abbreviated as DH). A multiple quantum well structure (MQW) consists of wells made of a small-bandgap material embedded in the active region of a DH. Band diagrams of a DH and MQW structure are schematically shown in Fig. 9. Carriers injected into the active regions of the DH or the MQW are confined to the well regions by the barriers. As a result, the thickness of the region in which carriers recombine is given by the thickness of the well rather than the diffusion length. The consequences of this change are significant. We assume that the thickness of the active region is much smaller than the typical diffusion length. Whereas diffusion lengths are several micrometers, the well region of a DH ranges from 0.1 to 1.0 μm. A MQW structure can have well regions as thin as 2 nm. Thus, carriers in a DH or MQW structure have higher carrier concentrations than carriers in homojunctions and a resulting higher radiative efficiency. To further prevent leakage of carriers out of the active region, blocking layers are used, as shown in Fig. 9. Because electrons are more mobile than holes, electron-blocking layers are more often used than hole-blocking layers.

Although DHs and MQWs allow for improved LED designs, there are also problems associated with such structures. One of the problems introduced by heterostructures is the resistance caused by the formation of a barrier at the heterointerface. Carriers transferring from one semiconductor to another must overcome this barrier by either tunneling or by thermal emission. The resistance caused by heterojunctions can have a strong deleterious effect on device performance, especially in high power devices. Fortunately, heterostructure band discontinuities can be completely eliminated by grading the chemical composition of the semiconductor in the vicinity of the heterostructure.

The *overflow of carriers* from the active region into the confinement regions is another loss mechanism. Carrier overflow occurs at high injection current densities. As the injection current increases, the carrier concentration in the active region increases. For sufficiently high current densities, the active region is flooded with carriers and the Fermi level may rise to the top of the barrier. As a result, the optical intensity saturates.

Carrier overflow of the active region is a potential problem in DH and MQW structures. In order to avoid this problem, high current LEDs must employ *thick* DH active regions, or *many* QWs for MQW active regions.

3.2. High Extraction Efficiency Structures

One of the most important problems facing high efficiency LEDs is the occurrence of trapped light within the semiconductor. Owing to the high refractive index of semiconductors, light incident on a planar semiconductor–air interface is totally internally reflected, if the angle of incidence is sufficiently large. Snell's law gives the critical angle of total internal reflection. This angle defines the escape cone. Light rays with a propagation direction that lies within the escape cone are able to leave the LED die. However, light trapped in the semiconductor will eventually be reabsorbed by a defect, the substrate, active region, or another absorbing layer.

If the light is absorbed by the substrate, the electron–hole pair will most likely recombine nonradiatively due to the inherently low efficiency of substrates. If the light is absorbed by the active region, the electron–hole pair may reemit a photon ("recycling" of a photon) or recombine nonradiatively. If reemitted as a photon, the photon propagation direction may fall into the escape cone. Thus the exact magnitude of the active region internal quantum efficiency and the probability of a photon to be emitted into the escape cone will determine the overall quantum efficiency of a device and the strategy (direct light extraction or light extraction by photon recycling) to attain higher efficiency. In the limit of low and high internal quantum efficiency, photon recycling is an ineffective and effective strategy to maximize power efficiency, respectively.

The occurrence of trapped light is illustrated in Fig. 10. A light ray emitted by the active region will be subject to total internal reflection, as predicted by Snell's law. In the high index approximation, the angle of total internal reflection is given by

$$\alpha_c = \bar{n}_s^{-1} \tag{31}$$

where $\bar{n}_s$ is the semiconductor refractive index and the critical angle α_c is given in radians. For high index semiconductors, the critical angle is quite small. For example, for the GaAs refractive index of 3.3, the critical angle for total internal reflection is only 17°. Thus most of the light emitted by the active region is trapped inside the semiconductor.

The light-escape problem has been known since the 1960s. It has also been known that the geometrical shape of the LED die plays a critical role. The optimum LED would be spherical in shape with a point-like light-emitting region in the center of the LED. Light emanating from the point-like active region is incident at a normal angle at the semiconductor–air interface. As a result, total internal reflection would not occur. Note, however, that the light is still subject to Fresnel reflection at the interface unless the sphere is coated with an antireflection coating. The most common LED structure has the shape of a rectangular parallelepiped. Such LED dies are fabricated by cleaving the wafer along its natural cleaving planes. The LEDs have a total of *six* escape cones, two of them perpendicular to the wafer surface, and four of them parallel to wafer surface (21). The bottom escape cone will be absorbed by the substrate if the substrate has a lower bandgap than the active region. The four in-plane escape cones will be at least partially absorbed by the substrate. Light in the top escape cone will be obstructed by the top contact, unless a thick current-spreading layer is employed. Thus the simple rectangular parallelepiped LED has low extraction efficiency. However, low manufacturing cost is an advantage.

There are different strategies to increase light extraction from LEDs including the resonant-cavity, surface-roughened, and die-shaped LED shown in Fig. 10**b**, **c**, and **d**, respectively. The resonant-cavity light-emitting diode (RCLED) has a light-emitting region inside an optical cavity (22,23). The optical cavity has a thickness of typically one-half or one times the wavelength of light, ie, a fraction of a micrometer for devices emitting in the visible or in the ir. The resonance wavelength of the cavity coincides with the emission wavelength of the active region. The spontaneous emission properties from a light-emitting region located inside the

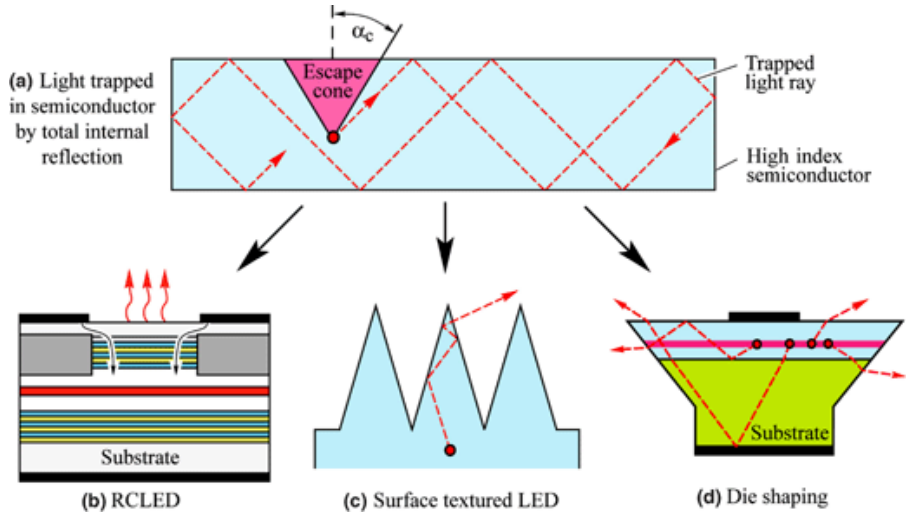

Fig. 10. (**a**) Light rays emanating from a point-like emitter are trapped inside the semiconductor due to total internal reflection. Only light rays with propagation directions falling within the escape cone can leave the semiconductor. Strategies increasing the extraction efficiency include (**b**) resonant-cavity, (**c**) textured, (**d**) die-shaped LEDs.

resonant cavity are enhanced by the change in optical mode density that has a maximum at or near the emission wavelength. The RCLED was the first practical device making use of spontaneous emission enhancement occurring in resonant cavities.

Other efficient ways to increase the light extraction efficiency include the use of *textured semiconductor surfaces* (see, eg, Refs. (24,25,26,27)) and the use of tapered output couplers (28,29,30). A cone-shaped surface-roughening is shown in Fig. 10**c**. Light rays emanating from the active region below the base of the cone undergo multiple reflections until they eventually have near-normal incidence at the semiconductor–air interface and escape from the die. For ir GaAs-based devices, external quantum efficiencies of 40% have been demonstrated with surface-textured LEDs and devices having tapered output couplers. A detailed discussion of properties and fabrication of microstructured surfaces was given by Sinzinger and Jahns (31).

Several die-shaped LEDs have been commercialized including the *pedestal-shaped die* shown in Figs. 11**a** and **b** and the *truncated inverted pyramid* (TIP) *die* shown in Figs. 11**c** and **d** (32). The ray traces indicated in the figures show that light rays at the base of the pyramid can escape from the semiconductor after undergoing one or multiple internal reflections. The TIP geometry reduces the mean photon path length within the crystal, and thus reduces internal losses. Ray tracing computer models are employed to optimize the sidewall angle θ to maximize light extraction.

The TIP LED is a high power LED with a large p–n junction area of $500 \times 500\ \mu$m. The luminous efficiency of TIP LEDs exceeds 100 lm/W and is one of the highest ever achieved with LEDs (32). A peak luminous efficiency of 102 lm/W was measured for orange-spectrum ($\lambda \approx 610$ nm) devices at an injection current of 100 mA. This luminous efficiency exceeds that of most fluorescent (50–104 lm/W) and all metal–halide (68–95 lm/W) lamps. In the amber color regime, the TIP LED provides a photometric efficiency of 68 lm/W ($\lambda \approx 598$ nm). This efficiency is comparable to the efficiency of high pressure sodium discharge lamps. A peak external quantum efficiency of 55% was measured for red-emitting ($\lambda \approx 650$ nm) TIP LEDs. Under pulsed operation (1% duty cycle), an efficiency of 60.9% was achieved, which sets a lower bound on the extraction efficiency of these devices (32).

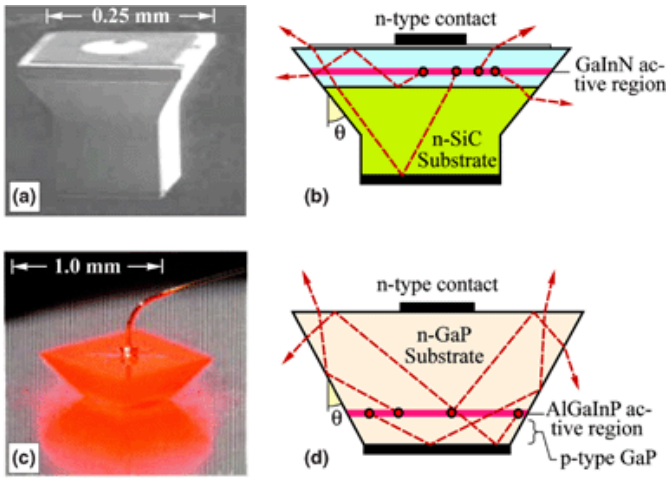

Fig. 11. Die-shaped devices: (**a**) Blue GaInN emitter on SiC substrate with trade name "Aton". (**b**) Schematic ray traces illustrating enhanced light extraction. (**c**) Micrograph of TIP AlGaInP/GaP LED. (**d**) Schematic diagram illustrating enhanced extraction. (Adopted from Ref. 32).

4. Resonant-Cavity Enhanced Structures

Spontaneous emission implies the notion that the recombination process occurs *spontaneously*, ie, without a means to influence this process. In fact, spontaneous emission has long been believed to be uncontrollable. However, research in microscopic optical resonators, where spatial dimensions are of the order of the wavelength of light, showed the possibility of controlling the spontaneous emission properties of a light-emitting medium. The changes of the emission properties include the spontaneous emission rate, spectral purity, and emission pattern. These changes can be employed to make more efficient, faster, and brighter semiconductor devices. The changes in spontaneous emission characteristics in resonant-cavity (RC) and photonic-crystal (PC) structures were reviewed by Joannopoulos (33).

Resonant-microcavity structures have been demonstrated with different active media and different microcavity structures. The first resonant-cavity structure was proposed by Purcell (1946) for emission frequencies in the radio frequency (rf) regime (34). Small metallic spheres were proposed as the resonator medium. However, no experimental reports followed Purcell's theoretical publication. In the 1980s and 1990s, several resonant cavity structures have been realized with different types of optically active media. The active media included organic dyes (35,36), semiconductors (37,38), rare-earth atoms (39,40), and organic polymers (41,42). In these publications, clear changes in spontaneous emission were demonstrated including changes in spectral, spatial, and temporal emission characteristics.

The simplest form of an optical cavity consists of two coplanar mirrors separated by a distance L_{cav}, as shown in Fig. 12. About one century ago, Fabry and Perot were the first to build and analyze optical cavities with coplanar reflectors (43). These cavities had a large separation between the two reflectors, ie, $L_{\text{cav}} \gg \lambda$. However, if the distance between the two reflectors is of the order of the wavelength, $L_{\text{cav}} \approx \lambda$, new physical phenomena occur, including the enhancement of the optical emission from an active material inside the cavity.

At the beginning of the 1990s, the *RCLED* was demonstrated, initially in the GaAs material system (44), shown in Fig. 13, and subsequently in organic light-emitting materials (41). Both publications reported an emission line narrowing due to the resonant cavities. The RCLEDs have many advantageous properties when compared with conventional LEDs, including higher brightness, increased spectral purity, and higher efficiency.

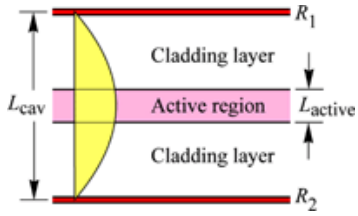

Fig. 12. Schematic illustration of a resonant cavity consisting of two metal mirrors with reflectivity R_1 and R_2. The active region has a thickness L_{active} and an absorption coefficient α. Also shown is the standing optical wave. The cavity length is L_{cav} is equal to $\lambda/2$.

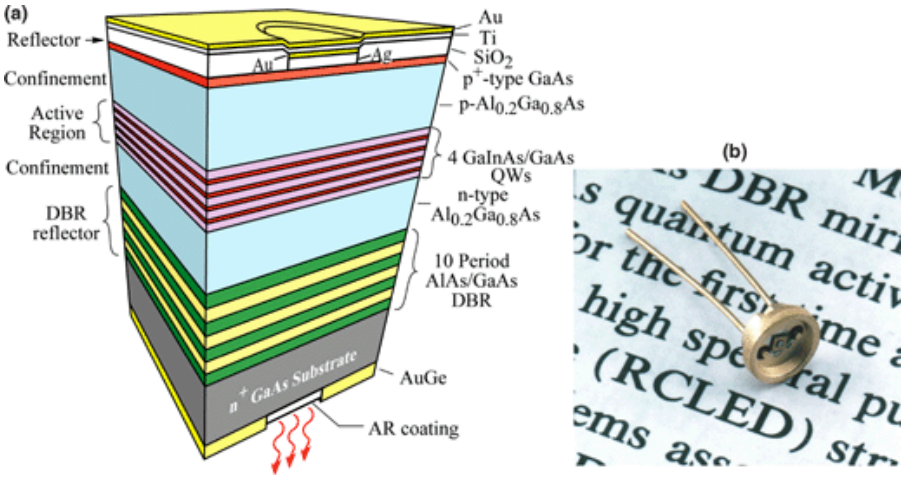

Fig. 13. (**a**) Schematic structure of a substrate-emitting GaInAs/GaAs RCLED consisting of a metal top reflector and a bottom distributed Bragg reflector (DBR). The RCLED emits at 930 nm. The reflectors are an AlAs/GaAs DBR and a Ag top reflector. (**b**) Picture of the first RCLED. (Adopted from Ref. 22).

For example, the RCLED spectral power density at the resonance wavelength was shown to be enhanced by more than one order of magnitude (45,46).

The enhancement of spontaneous emission can be calculated based on the changes of the *optical mode density* in a one-dimensional (1D) resonator, ie, a coplanar Fabry–Perot cavity. We first discuss the basic physics causing the changes of the spontaneous emission from an optically active medium located inside a microcavity and give analytical formulas for the spectral and integrated emission enhancement. The spontaneous radiative transition rate in an optically active, homogeneous medium is given by (see, eg, Ref. 47).

$$W_{spont} = \tau_{spont}^{--1} = \int_0^\infty W_{spont}^{(\ell)} \rho(\nu\ell)\, d\nu\ell \tag{32}$$

where $W_{spont}{}^{(\ell)}$ is the spontaneous transition rate into the optical mode ℓ and $\rho(\nu\ell)$ is the optical mode density. Assuming that the optical medium is homogeneous, the spontaneous emission lifetime, τ_{spont}, is the inverse of the spontaneous emission rate. However, if the optical mode density in the device depends on the spatial direction, as in the case of a cavity structure, then the emission rate given in equation 32 depends on the direction. Equation 32 can be applied to some small range of solid angle along a certain direction, eg, the

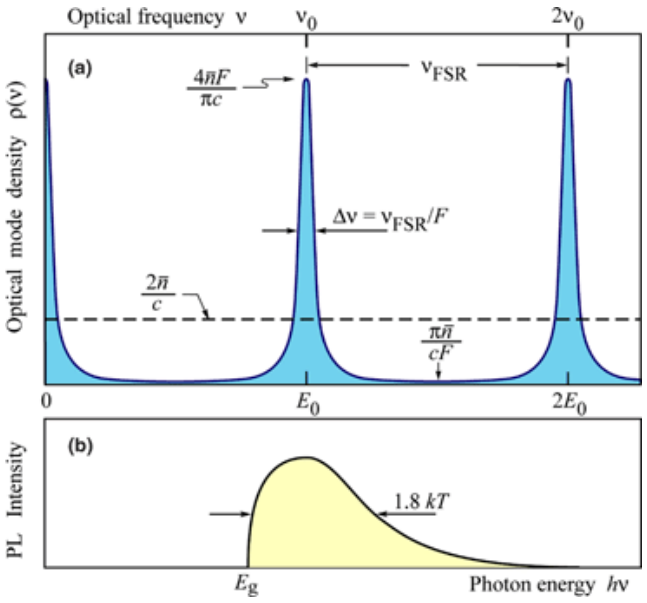

Fig. 14. (**a**) Optical mode density of a 1D planar microcavity (solid line) and of homogeneous 1D space. (**b**) Theoretical shape of the luminescence spectrum of bulk semiconductors.

direction perpendicular to the reflectors of a Fabry–Perot cavity. Thus, equation 32 can be used to calculate the emission rate along a specific direction, in particular the optical axis of a cavity.

The spontaneous emission rate into the optical mode ℓ,$W^{(\ell)}_{\text{spont}}$, contains the dipole matrix element of the two electronic states involved in the transition (47). Thus $W^{(\ell)}_{\text{spont}}$ will *not* be changed by placing the optically active medium inside an optical cavity. However, the optical mode density, $\rho(\nu\ell)$, is strongly modified by the cavity. Next, the changes in optical mode density will be used to calculate the changes in spontaneous emission rate.

First we compare the optical mode density in free space with the optical mode density in a cavity. For simplicity, we restrict our considerations to the 1D case, ie, to the case of a coplanar Fabry–Perot cavity. Furthermore, we restrict our considerations to the emission along the optical axis of the cavity.

In a 1D homogeneous medium, the density of optical modes per unit length per unit frequency is given by

$$\rho^{1D}(\nu) = \frac{2\,n}{c} \tag{33}$$

where n is the refractive index of the medium. Equation 33 can be derived using a similar formalism commonly used for the derivation of the mode density in free space. The constant optical mode density given by equation 33 is shown in Fig. 14.

In planar cavities, the optical modes are discrete and the frequencies of these modes are integer multiples of the fundamental mode frequency as shown schematically in Fig. 14. The fundamental and first excited mode occur at frequencies of ν_0 and $2\nu_0$, respectively. For a cavity with two metallic reflectors (no distributed Bragg reflectors) and a π phase shift of the optical wave upon reflection, the fundamental frequency is given by $\nu_0 = c/2nL_{\text{cav}}$, where c is the velocity of light in vacuum and L_{cav} is the length of the cavity. In a *resonant cavity*, the emission frequency of an optically active medium located inside the cavity equals the frequency of one of the cavity modes.

The optical mode density along the cavity axis can be derived using the relation between the mode density in the cavity and the optical transmittance through the cavity, $T(\nu)$,

$$\rho(\nu) = K\,T(\nu) \tag{34}$$

where K is a constant. The value of K can be determined by a normalization condition, ie, by considering a single optical mode. The transmittance through a Fabry–Perot cavity can be written as

$$T(\nu) = \frac{T_1\,T_2}{1+R_1\,R_2 - 2\sqrt{R_1\,R_2}\cos\left(4\pi\bar{n}L_{\text{cav}}\nu/c\right)} \tag{35}$$

The transmittance has maxima at $\nu = 0$, ν_0, $2\nu_0$, ..., and minima at $\nu = \nu_0/2$, $3\nu_0/2$, $5\nu_0/2$, ... The optical mode density of a 1D cavity for emission along the cavity axis is given by

$$\rho(\nu) = \frac{(R_1\,R_2)^{3/4}}{T_1\,T_2}\,\frac{4n}{c}(1-\sqrt{R_1\,R_2})T(\nu) \tag{36}$$

This equation allows one to calculate the density of optical modes at the maxima and minima. At the *maxima*, the mode density is given by

$$\rho_{\max} = \frac{(R_1\,R_2)^{3/4}}{1-\sqrt{R_1\,R_2}}\,\frac{4n}{c} \tag{37}$$

Because the emission rate at a given wavelength is directly proportional to the optical mode density, the emission rate *enhancement spectrum* is given by the ratio of the 1D cavity mode density to the 1D free space mode density. The enhancement factor at the resonance wavelength is thus given by the ratio of the optical mode densities with and without a cavity, ie,

$$G_{\text{e}} = \frac{\rho_{\max}}{\rho^{1D}} \approx \frac{2}{\pi}F \approx \frac{2}{\pi}\,\frac{\pi(R_1\,R_2)^{1/4}}{1--R_1\,R_2} \tag{38}$$

The equation shows that a strong enhancement of the spontaneous emission rate along the cavity axis can be achieved with microcavities.

Equation 38 represents the *average* emission rate enhancement out of *both* reflectors of the cavity. To find the enhancement out a *single* direction, we multiply the enhancement given by equation 38 by the fraction of the light exiting the mirror with reflectivity R_1 (ie, $1-R_1$) divided by the average loss of the two mirrors for one round trip in the cavity {ie, $(0.5)[(1-R_1)+(1-R_2)]$}. For large R_1 and R_2, this consideration gives for the enhancement of the emission exiting R_1

$$G_{\text{e}} \approx \frac{2(1-R_1)}{2-R_1-R_2}\,\frac{2F}{\pi} \approx \frac{1-R_1}{1-\sqrt{R_1\,R_2}}\,\frac{2F}{\pi} \approx \frac{2}{\pi}\,\frac{\pi(R_1\,R_2)^{1/4}(1-R_1)}{(1-\sqrt{R_1\,R_2})^2} \tag{39}$$

where we used the approximation $1-(R_1\,R_2)^{1/2} \approx (0.5)(1-R_1\,R_2) \approx (0.5)(2-R_1-R_2)$. Equation 39 represents the emission rate enhancement from a *single* reflector with reflectivity R_1. The total enhancement *integrated over wavelength*, rather than the enhancement at the resonance wavelength, is relevant for many practical devices. *On resonance*, the emission is enhanced along the axis of the cavity. However, for sufficiently far *off resonance*, the emission is suppressed. Because the natural emission spectrum of the active medium

(without a cavity) can be much broader than the cavity resonance, it is, *a priori*, not clear whether the integrated emission is enhanced. To calculate the wavelength-integrated enhancement, the spectral width of the cavity resonance and the spectral width of the natural emission spectrum must be determined. The resonance spectral width can be calculated from the finesse of the cavity or the cavity quality factor.

The theoretical width of the emission spectrum of bulk semiconductors is 1.8 kT (see, eg, Ref. 48), where k is Boltzmann's constant and T is the absolute temperature. At room temperature, 1.8 kT corresponds to an emission line width of $\Delta\lambda_n = 31$ nm for an emission wavelength of 900 nm. For a cavity resonance width of 5–10 nm, one part of the spectrum is strongly enhanced, whereas the rest of the spectrum is suppressed. The integrated enhancement ratio (or suppression ratio) can be calculated analytically by assuming a Gaussian natural emission spectrum. For semiconductors at 300 K, the line width of the natural emission is, in the case of high finesse cavities, *larger* than the width of the cavity resonance. The Gaussian emission spectrum has a width of $\Delta\lambda_n = 2\sigma\ (2\ \ln\ 2)^{1/2}$ and a peak value of $[\sigma\ (2\pi)^{1/2}]^{-1}$, where σ is the standard deviation of the Gaussian function. The integrated enhancement ratio (or suppression ratio) is then given by (49)

$$G_{\text{int}} = \frac{\pi}{2} G_e \Delta\lambda \frac{1}{\sigma\sqrt{2\,\pi}} = G_e \sqrt{\pi\ \ln 2} \frac{\Delta\lambda}{\Delta\lambda_n} \tag{40}$$

where the factor of $\pi/2$ is due to the Lorentzian line shape of the enhancement spectrum. Hence, the integrated emission enhancement depends on the natural emission line width of the active material. The value of G_{int} can be quite different for different types of optically active materials. Narrow atomic emission spectra can be enhanced by several orders of magnitude (40). On the other hand, materials having broad emission spectra such as dyes or polymers may not exhibit any integrated enhancement at all. Equation 40 also shows that the width of the resonance has a profound influence on the integrated enhancement (35,36). Narrow resonance spectral widths, ie, high finesse values or long cavities, reduce the integrated enhancement (45).

The relation between the overlap of the spontaneous emission spectrum and the cavity length is illustrated in Fig. 15, which shows the optical mode density of a short and a long cavity. Both cavities have the same mirror reflectivities and finesse. The natural emission spectrum of the active region is shown in Fig. 15**c**. The best overlap between the resonant optical mode and the active region emission spectrum is obtained for the *shortest* cavity. Thus a cavity length of $\lambda/2$ provides the largest enhancement.

The largest enhancements are achieved with the shortest cavities, which in turn are obtained if the *fundamental* cavity mode is in resonance with the emission from the active medium. The cavity length is shortest for metallic reflectors. The DBRs with a short penetration depth, ie, DBRs consisting of two materials with a large difference in refractive index, also reduce the cavity length.

The reflection and emission properties of the RCLED are shown in Fig. 16**a** and **b**. The reflection spectrum of the RCLED exhibits a highly reflective band for wavelengths >900 nm and a dip in the reflectivity at the cavity resonance. The spectral width of the cavity resonance is 6.3 nm. The emission spectrum of an electrically pumped device, shown in Fig. 16**b**, has nearly the same shape and width as the cavity resonance.

In conventional LEDs, the spectral characteristics of the devices reflect the thermal distribution of electrons and holes in the conduction and valence band. The spectral characteristics of light emission from microcavities are as intriguing as they are complex. However, restricting our considerations to the optical axis of the cavity simplifies the cavity physics considerably. If we assume that the cavity resonance is much narrower than the natural emission spectrum of the semiconductor, then the on-resonance luminescence is enhanced, whereas the off-resonance luminescence is suppressed. The on-axis emission spectrum should therefore reflect the enhancement, ie, the resonance spectrum of the cavity. The experimental results shown in Fig. 16 confirm this conjecture.

Particularly high spontaneous emission enhancements can be attained with emitters that have very narrow emission lines. Atomic transitions, eg, in rare-earth elements have such narrow emission lines. For this reason, rare-earth doped cavities are a prime example of the emission enhancement provided by resonant

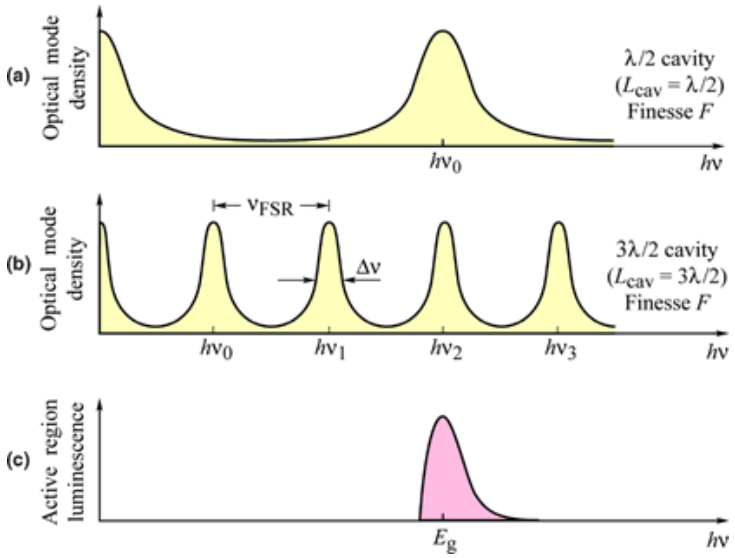

Fig. 15. Optical mode density for (**a**) a short and (**b**) a long cavity with the same finesse F. (**c**) Spontaneous free space emission spectrum of an LED active region. The spontaneous emission spectrum has a better overlap with the short-cavity mode spectrum compared with the long-cavity mode spectrum.

cavities. The emission spectrum of an Erbium-doped Si/SiO_2 resonant cavity is shown in Fig. 17 (40). A distinct narrowing of the Er emission spectrum is found for emission along the optical axis. A huge emission enhancement with cavity is found, a factor >50, when compared to a noncavity structure.

The peak emission wavelength depends on the emission angle with respect to the surface normal (polar angle). Denoting the polar emission angle in air as Θ_0, the emission wavelength is given by

$$\lambda_e = \lambda_{res} \cos\left[\arcsin\left(\frac{1}{n}\sin\Theta_0\right)\right] \tag{41}$$

where λ_{res} is the resonance wavelength of the cavity. For small angles, the equation can be approximated by

$$\lambda_e \approx \lambda_{res}\left(1 - \frac{\Theta_0^2}{2n^2}\right) \tag{42}$$

where the refractive index n is the effective refractive index of the medium. The angular dependence of the peak emission wavelength is shown in Fig. 18. The dashed line is the approximate solution of equation 42. A refractive index of 1.5 has been used in this calculation.

The RCLED is a commercial product that is manufactured in large quantities. Primary applications are in signage and communication. The devices are particularly well suited for plastic optical fiber systems. The directed emission pattern improves LED-fiber coupling efficiency. The narrow emission line reduces material and chromatic dispersion effects. As a result, RCLEDs enable longer transmission distances and simultaneously higher data rates. The enhanced coupling and narrow emission line of the fiber-coupled intensity is shown in Fig. 19. Inspection of the figure reveals the much higher power coupled to a fiber and the narrower emission spectrum of the RCLED.

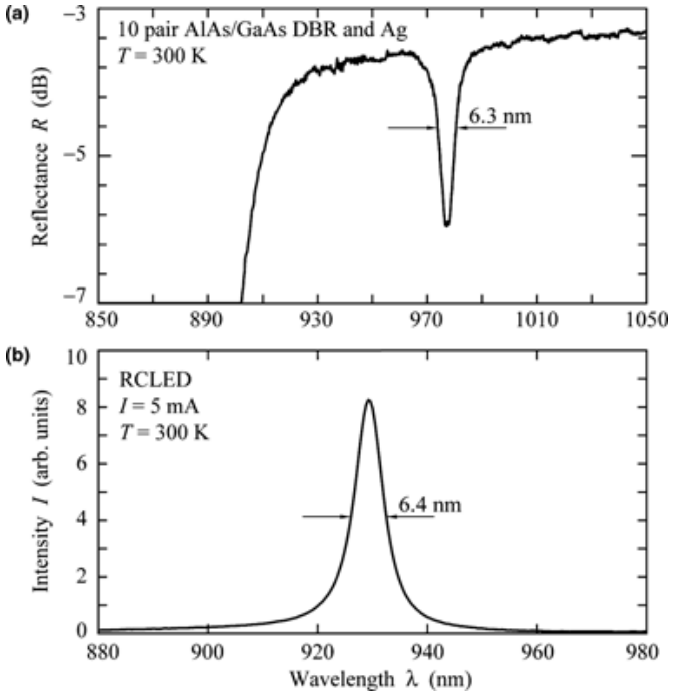

Fig. 16. (**a**) Reflectance of a resonant cavity consisting of a 10-pair AlAs/GaAs distributed Bragg reflector and an Ag reflector. (**b**) Emission spectrum of a RCLED consisting of a 10-pair AlAs/GaAs distributed Bragg reflector and an Ag reflector. (Adopted from Ref. 22).

5. Omnidirectional Reflectors

There are several different ways to obtain highly reflective coatings in the visible wavelength region. Metallic layers provide robust reflectors capable of reflecting visible light over a wide range of wavelengths and incident angles. Metals reflect visible light since this frequency range is well below typical plasma frequencies of the free electron gas. However, electron oscillations induced by incident light waves not only result in reflection, but also in absorption caused by electron–phonon scattering.

Distributed-Bragg reflectors (DBRs) are periodic structures with a unit cell of two dielectric layers having different refractive indexes n_i and thicknesses d_i ($i = 1, 2$). The DBRs can be regarded as 1D photonic crystals with a high reflectivity stop band (photonic-crystal gap) comprising the nonpropagating light states in the crystal. The DBRs are usually designed to have a certain center wavelength λ_{center} at perpendicular incidence. However, the DBR reflectivity depends on the incidence angle θ such that the stop band shifts toward shorter wavelengths for increasing θ without changing its spectral width (51). As a result, DBRs become transparent for oblique angles of incidence.

The reflection properties of metals and DBRs depend on the polarization of the incident lightwave. According to Brewster's law, the reflection of light polarized parallel to the plane of incidence (TM-mode) has a minimum at the incidence angle

$$\tan\theta_B = \frac{n_1}{n_2} \tag{43}$$

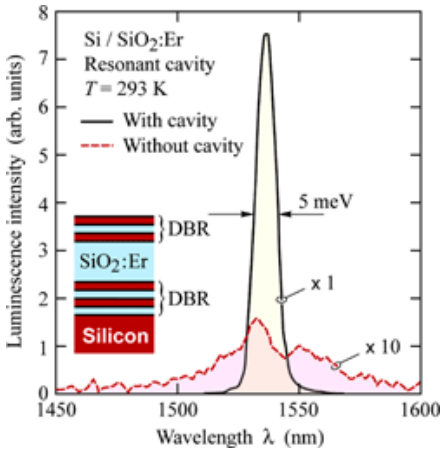

Fig. 17. Photoluminescence spectra of Er-doped SiO_2. One of the spectra is for the Er-doped SiO_2 located in a cavity resonant at 1540 nm. The other spectrum is without a cavity. The emission enhancement factor is 50. (Adopted from Ref. 40).

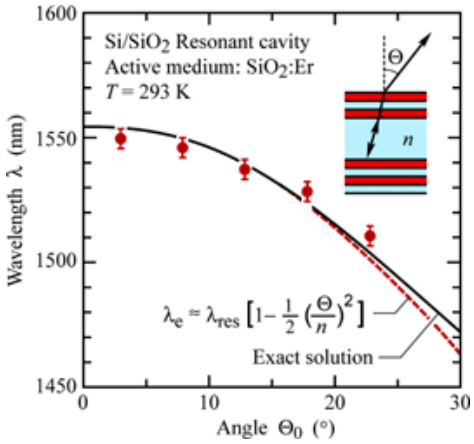

Fig. 18. Emission wavelength as a function of angle for a planar resonant cavity. (Adopted from Ref. 40).

where n_1 and n_2 are the refractive indexes of the adjacent materials. This is particularly important for DBRs, which exhibit a drastic reflectivity decrease at θ_B. The DBRs with improved wide-angle reflectivity can be achieved, eg, by using *aperiodically* stacked layers with thickness gradients or random thickness distributions (52,53). Much research was devoted to DBRs with a *complete* photonic-crystal bandgap represented by a certain frequency range where all incoming photons regardless of their momentum vector $\hbar\vec{k}$ are reflected. These omnidirectional reflectors (ODRs) have a wide range of interesting applications such as all-dielectric coaxial waveguides (54), omnidirectional mirror fibers (55), and light transport tubes (56).

Omnidirectional reflection characteristics can also be obtained with distributed Bragg reflectors that have a very high index contrast such as Si/SiO_2. Another approach used polystyrene and tellurium layers in a DBR (57). Due to the large difference of the refractive indexes, $n_{SiO_2} = 1.45$; $n_{polystyrenene} = 1.8$; $n_{Si} = 3.5$; $n_{Te} = 5$, the Brewster angle θ_B is much larger than the critical angle θ_c for total reflection resulting in a nearly complete photonic-crystal bandgap in the wavelength range from 10 to 15 μm. Still another approach consists of the use

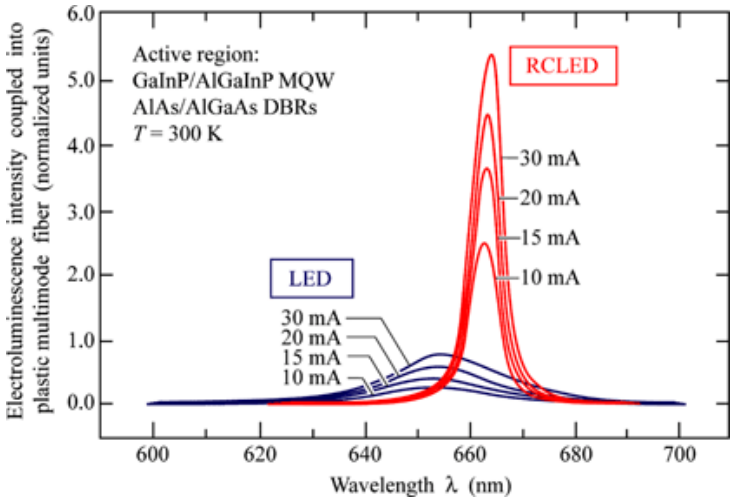

Fig. 19. Spectra of light coupled into a plastic optical fiber from an GaInP/AlGaInP MQW RCLED and a conventional GaInP/AlGaInP LED at different drive currents. Note the narrower spectrum and higher coupled power of the RCLED. (Adopted from Ref. 50).

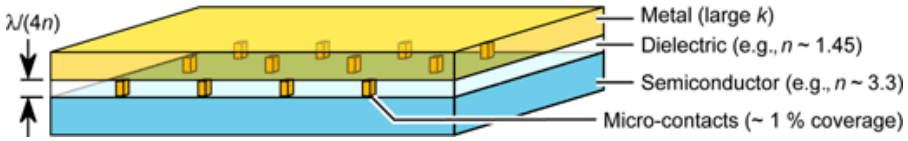

Fig. 20. Perspective view of an omnidirectional reflector (ODR). The ODR also serves as ohmic contact.

of birefringent polymers in DBRs with two different refractive indexes parallel and vertical to the DBR layer planes (56). By adjusting the differences between the vertical and in-plane indices the value of the Brewster angle can be controlled. Brewster angles up to 90° (grazing incidence) and even imaginary values are possible resulting in high reflectivity for TM-polarized light at virtually all incident angles.

Unfortunately, the applicability of the above-mentioned omnidirectional DBRs in LEDs is limited since they are electrically insulating. In addition, these omnidirectional DBR structures present a considerable thermal barrier preventing efficient heat sinking due to their large thermal resistance and thickness. The DBRs have been used as substrate coating to enhance the light extraction (58,59). However, the active region of a LED emits light isotropically, and therefore the poor reflectivity of the regular DBRs at oblique incidence angles results in undesired losses particularly for wave-guided modes as discussed above.

A very promising electrically conductive omnidirectional reflector suitable for use in LEDs is shown in Fig. 20 (60,61). The reflector comprises the LED semiconductor material with a refractive index n_s, a low refractive index layer (n_{li}), and a metal with a complex refractive index $N_m = n_m + i\ k_m$, where k_m is the extinction coefficient.

The low index layer is perforated by many small ohmic contacts that cover only a small fraction of the entire area. The array of microcontacts allows the electrical current to pass through the dielectric layer. Assuming that the ohmic contacts have an area of 1% of the reflector, and that the alloyed ohmic contact metal is 50% reflective, the reflectivity of the ODR is reduced by only 0.5%. The ODR described here can be used with low cost Si-substrates or metal substrates using conductive epoxy or a metal-to-metal bonding process. These

bonding processes have much less stringent requirements than direct semiconductor-to-semiconductor wafer bonding processes.

The reflectance of the semiconductor/metal reflector (eq. 43) as a function of the incident angle θ is given by (62)

$$R_{\mathrm{TE}} = |\frac{n_s \cos\theta_1 - N_m \cos\theta_2}{n_s \cos\theta_1 + N_m \cos\theta_2}|^2 \tag{44}$$

$$R_{\mathrm{TM}} = |\frac{\frac{n_s}{\cos\theta_1} - \frac{N_m}{\cos\theta_2}}{\frac{n_s}{\cos\theta_1} + \frac{N_m}{\cos\theta_2}}|^2 \tag{45}$$

The reflectance of the triple-layer ODR (eq. 45) as a function of the incident angle θ (see Fig. 21) is given by (62)

$$R = |\frac{r_{01} + r_{12}\exp(2i\phi)}{1 + r_{01} \cdot r_{12}\exp(2i\phi)}|^2 \tag{46}$$

where,

$$r_{01\mathrm{TE}} = \frac{n_s \cos\theta_1 - n_{li} \cos\theta_2}{n_s \cos\theta_1 + n_{li} \cos\theta_2} \tag{47}$$

$$r_{01\mathrm{TM}} = \frac{n_{li} \cos\theta_1 - n_s \cos\theta_2}{n_{li} \cos\theta_1 + n_s \cos\theta_2} \tag{48}$$

$$r_{12\mathrm{TE}} = \frac{n_{li} \cos\theta_2 - N_m \cos\theta_3}{n_{li} \cos\theta_2 + N_m \cos\theta_3} \tag{49}$$

$$r_{12\mathrm{TM}} = \frac{N_m \cos\theta_2 - n_{li} \cos\theta_3}{N_m \cos\theta_2 + n_{li} \cos\theta_3} \tag{50}$$

and

$$\phi = \frac{2\pi}{\lambda} n_{\mathrm{li}} h \cos\theta_2 \tag{51}$$

Equations 45 apply to a low index dielectric layer thickness of $\lambda_0/(4n_{\mathrm{li}})$, ie, to a quarter wavelength layer. Figure 21**b** shows the reflectivity $R(\theta)$ at $\lambda = 470$ nm of triple layer ODR (GaN/SiO_2/Ag), metal reflectors (GaN/Ag and GaN/Ni/Au), and 20 periods of $Al_{0.25}Ga_{0.75}N$/GaN DBR. The reflectivity curves were calculated using the optical transfer matrix method (51,62) and using parameters, $n_{\mathrm{Ag}} = 0.132$, $k_{\mathrm{Ag}} = 2.72$, $n_{\mathrm{SiO_2}} = 1.46$, $n_{\mathrm{GaN}} = 2.45$ at 470 nm (63). As opposed to the ODR and metal reflectors, $R(\theta)$ of the DBR sharply drops $>14^\circ$ and recovers only at angles close to grazing incidence. Note that the reflectivity for TE-polarized light of the GaN/SiO_2/Ag ODR is higher than that of the GaN/Ag reflector for all angles of incidence.

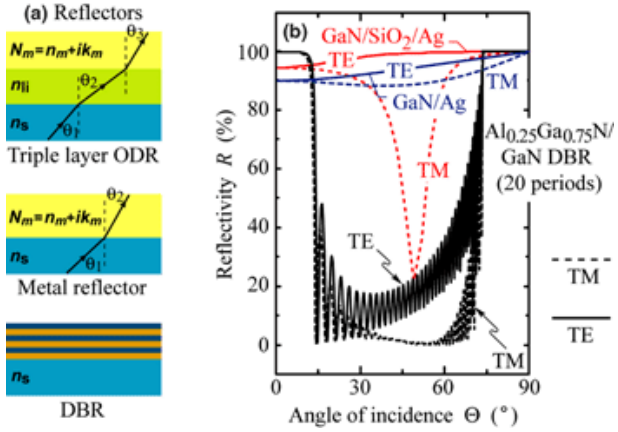

Fig. 21. (**a**) Reflector types including triple layer ODR, metal reflector, and DBR. (**b**) Calculated reflectivities of GaN/SiO_2/Ag ODR and of AlGaN/GaN DBR. (Adopted from Ref. 61). Dashed and solid lines indicate reflectivities of TM- and TE-lightwaves, respectively.

Because the LED active region emits light isotropically, the total substrate reflectivity averaged over the solid angle would be a suitable figure-of-merit. The average reflectivity is given by

$$\bar{R}(\lambda) = \frac{1}{2\pi} \int_0^{\pi/2} R(\lambda,\theta)\, 2\pi \sin\theta \, \mathrm{d}\theta \tag{52}$$

where λ denotes the emission wavelength and θ the angle of incidence in the semiconductor. As a result, the angle averaged reflectivity $\bar{R}$ is much larger for a GaN/SiO_2/Ag ODR ($\bar{R} = 0.93$ at $\lambda = 470$ nm) and Ag reflector ($\bar{R} = 0.92$ at $\lambda = 470$ nm) than for the DBR ($\bar{R} = 0.49$ for TE-polarized, $\bar{R} = 0.38$ for TM-polarized at $\lambda = 470$ nm). The averaged reflectivity of triple-layer ODRs exceeds the value of $\bar{R}$ for the transparent DBR by about a factor of 2.

Note that the reflectivity increase is significant. The power of a wave-guided mode, P, attenuated by multiple reflection events (with reflectivity R) depends on the number of reflection events, N, according to

$$P = P_0 R^N \tag{53}$$

where P_0 is the initial power of the mode.

At perpendicular incidence, the reflectance of the triple-layer ODR is given by (60,61)

$$R_{\mathrm{ODR}}(\theta_1 = 0) = \frac{\{(n_{\mathrm{S}} - n_{\mathrm{li}})(n_{\mathrm{li}} + n_{\mathrm{m}}) + (n_{\mathrm{S}} + n_{\mathrm{li}})k_{\mathrm{m}}\}^2 + \{(n_{\mathrm{S}} - n_{\mathrm{li}})k_{\mathrm{m}} + (n_{\mathrm{S}} + n_{\mathrm{li}})(n_{\mathrm{li}} - n_{\mathrm{m}})\}^2}{\{(n_{\mathrm{S}} + n_{\mathrm{li}})(n_{\mathrm{li}} + n_{\mathrm{m}}) + (n_{\mathrm{S}} - n_{\mathrm{li}})k_{\mathrm{m}}\}^2 + \{(n_{\mathrm{S}} + n_{\mathrm{li}})k_{\mathrm{m}} + (n_{\mathrm{S}} - n_{\mathrm{li}})(n_{\mathrm{li}} - n_{\mathrm{m}})\}^2} \tag{54}$$

For an AlGaInP/SiO_2/Ag structure emitting at $\lambda = 630$ nm, Eq. 48 yields a normal-incidence reflectance $R_{\mathrm{ODR}}(\theta = 0) > 98\%$. This value exceeds the corresponding value for a structure *without* low index layer by ~3%, thereby reducing optical losses by a substantial amount. Due to the power-law dependence this improvement of R is of great importance and shows the huge potential of ODRs. The triple-layer ODR can be improved significantly by using novel low n materials such as nano-porous SiO_2, which has a refractive index as low as 1.10 (64). It is transparent in the visible and near-uv spectrum. In contrast, SiO_2 has a refractive index of ~1.46 and very good transparency in the visible and near-uv spectrum.

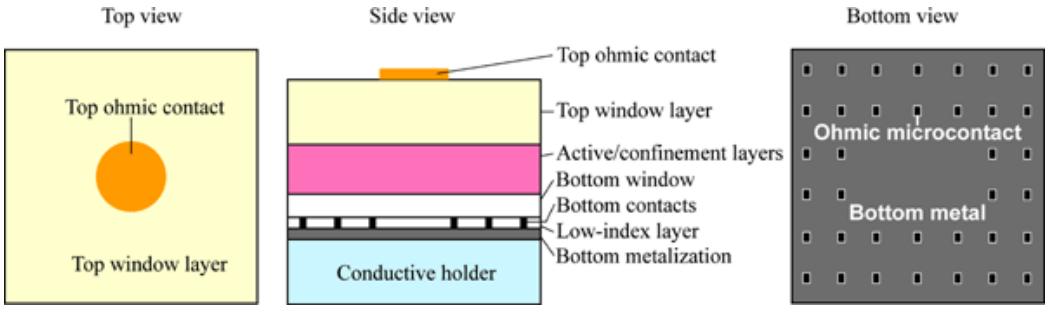

Fig. 22. Schematic of the omnidirectional reflector (ODR) LED. An array of microcontacts perforating the ODR serves as p-type ohmic contact to the epitaxial AlGaInP layers.

The schematic structure of an ODR-based LED a shown in Fig. 22. It consists of a top current-spreading (or window) layer, the active and confinement layers, a bottom window layer, the ODR, and a submount such as a Si or metal wafer. The active layers include the lower and upper confinement layers and the bulk or MQW active region. The wafer is grown in the standard "p-side up" mode that is employed in nearly all LEDs at the present time.

The wide-angle reflectivity of the ODR allows wave guiding of light rays with much smaller attenuation than a DBR. As a result, light extraction at the edges of the LED die is strongly increased.

6. White LED

Semiconductor-based light sources have, in principle, the potential to achieve near-unit power efficiency. This is in contrast to conventional light sources such as incandescent and fluorescent lamps that have fundamental efficiency limitations. Due to their high efficiency potential, semiconductor light sources are expected to replace fluorescent and inefficient incandescent sources.

Color rendering, luminous efficacy and luminous efficiency are important criteria for white light sources used for daylight illumination applications. *Color rendering* can be thought of as the ability of a light source to show the true colors of an object. The color rendering index (CRI) quantitatively measures the ability of an illumination source to render all the colors of an object illuminated by that source. The maximum value of the CRI is 100 and this value implies the best possible color rendering. The color rendering capability of a white light source is determined by the emission spectrum. High fidelity color rendering can be best achieved with a broadband source emitting over the entire visible spectrum.

The *luminous efficacy of radiation* measured in units of lumens per watt (lm/W) is the conversion efficiency from optical power to luminous flux. Green light at 555 nm has the highest luminous efficacy. At that wavelength, the human eye is most sensitive. The *luminous efficiency of the source*, also measured in units of lm/W, is the luminous flux of a light source divided by the electrical input power. The luminous efficiency of the source is an important figure-of-merit for monochromatic and white light sources.

It has been shown that there is a fundamental trade-off between color rendering and luminous efficacy (65). Daylight illumination sources with high luminous efficacy necessarily have poor color rendering properties. Daylight illumination sources with excellent color rendering necessarily have lower luminous efficacy. In the case of dichromatic, LED-based white light sources, the luminous efficacy can be very high (>400 lm/W). Therefore, these light sources are suitable for signage application, but their concomitant low color rendering properties are undesirable in daylight illumination applications. The color rendering properties can be improved by choosing green GaInN-based LEDs with relatively broad emission spectra.

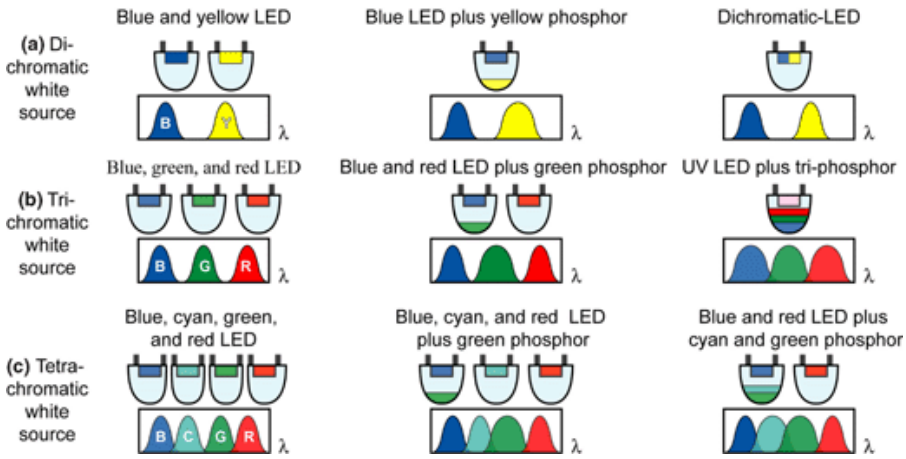

Fig. 23. The LED-based approaches for white light sources and corresponding optical spectra. The highest luminous efficacy is provided by the dichromatic approaches. The best color rendering is obtained with tetrachromatic approaches. Trichromatic approaches based on LEDs can provide good color rendering as well as high luminous efficacy.

Different semiconductor-based schemes to generate white light are shown in Fig. 23. The figure shows (a) dichromatic, (b) trichromatic, and (c) tetrachromatic white sources including single-chip semiconductor sources and multichip semiconductor sources. The figure also shows semiconductor–phosphor-based sources including a blue LED/yellow phosphor source, a blue and red LED/green phosphor source, and a uv LED/phosphor source. Tetrachromatic approaches offer outstanding color rendering properties. As a result, there is little motivation to develop pentachromatic approaches.

Several characteristics of the trichromatic sources shown in Fig. 23 are noteworthy. Trichromatic approaches based on either LEDs or phosphors provide excellent color rendition with a CIE general color rendering index of 90 or higher (66). Due to the unavoidable Stokes shift in the trichromatic uv–LED/phosphor source, the potential luminous efficiency of this source is lower compared with a trichromatic multichip LED approach. The trichromatic approach shown in Fig. 23 consisting of a blue LED, a green phosphor, and a red LED is motivated by the unavailability of highly efficient green semiconductor-based emitters. The use of the red LED is motivated by the availability of efficient red AlGaInP LEDs. In addition, the employment of red LEDs allows for the avoidance of the very large Stokes shift concomitant with the uv or blue LED/red phosphor combination. Therefore, the two LED/green phosphor approach promises both, good efficiency and color rendering capabilities.

7. Packaging

Virtually all LEDs are encapsulated with an optically transparent polymer. Encapsulants have several requirements including high transparency, high refractive index, chemical stability, high temperature stability, and hermeticity. The refractive index contrast between the semiconductor and air is reduced by the encapsulant. A reduced index contrast at the semiconductor surface increases the angle of total internal reflection thereby enlarging the LED escape cone and extraction efficiency. Furthermore, encapsulants provide protection against unwanted mechanical shock, humidity, and chemicals. The encapsulant also stabilizes the LED die and bonding wires. Finally, the epoxy resin provides mechanical stability to the two metal leads of the LED and holds them in place.

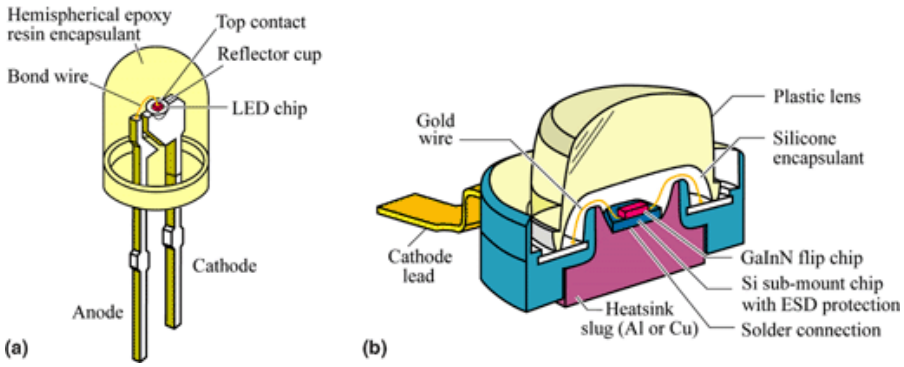

Fig. 24. (**a**) The LED with hemispherical encapsulant. (**b**) Cross-section through high power package. The heatsink slug can be soldered to a printed circuit board for efficient heat removal. (Adopted from Ref. 67).

A ***low power package*** is shown in Fig. 24**a**. The device is attached to the bottom of a cup-like depression (reflector cup) formed in one of the lead wires (usually the cathode lead). A bond wire connects the LED top contact to the other lead wire (usually the anode lead). The LED package shown in the figure is frequently referred to as a "5 mm" or "T1-3/4" package. In low power LEDs, the encapsulant has the shape of a hemisphere, so that the angle of incidence at the encapsulant–air interface is always normal. As a result, total internal reflection does not occur at the encapsulant–air interface.

A ***power package*** is shown in Fig. 24**b**. Power packages have a *thermally conductive path* from the LED die, through the package, to a heat sink, eg, a printed circuit board. The power package shown in the figure has several advanced features. First, the package contains an Al or Cu heatsink slug with low thermal resistivity. Second, the die is encapsulated with silicone. Because standard silicone retains mechanical softness in its cured state, the silicone encapsulant is covered with a plastic cover that also serves as lens. Third, the die is directly mounted on a Si submount that includes electrostatic discharge (ESD) protection (68). Electrostatic discharge-protection circuits typically consist of a series of Si diodes or of a Si Zener diode. The current caused by an electrostatic discharge, which can be understood as a short high voltage pulse applied to the electrodes of the device, will bypass the LED and flow mostly through the series of low resistance Si diodes thereby protecting the LED.

The thermal resistance of LED packages together with the maximum temperature of operation determines the maximum thermal power that can be dissipated in the package. The maximum temperature of operation may be determined by reliability considerations, by the degradation of the encapsulant, and by internal-quantum-efficiency considerations. Several types of LED packages and their thermal resistance are shown in Fig. 25 (69). Early LED packages introduced in the late 1960s and still used for low power packages, have a high thermal resistance of ∼240 K/W. Packages using ***heatsink slugs*** made of Al or Cu that transfer heat from the die directly to a printed circuit board (PCB), which in turn spreads the heat, have thermal resistances of 6–12 K/W. It is expected that thermal resistances of <5 K/W will be achieved for advanced passively cooled power packages.

Note that the packages shown in Fig. 25 do not use *active cooling* (fan cooling). Heatsinks with cooling fins and fan have thermal resistances <0.5 K/W and are commonly used to cool electronic microchips, eg, Si CMOS microprocessors. The use of active cooling devices would reduce the power efficiency of LED-based systems and are therefore not used.

A common encapsulant is ***epoxy resin*** (also called epoxy), which remains transparent and does not show degradation over many years for long-wavelength visible spectrum and ir LEDs. However, it has been reported that epoxy resins lose transparency in LEDs emitting at shorter wavelengths, ie, in the blue, violet, and uv (70).

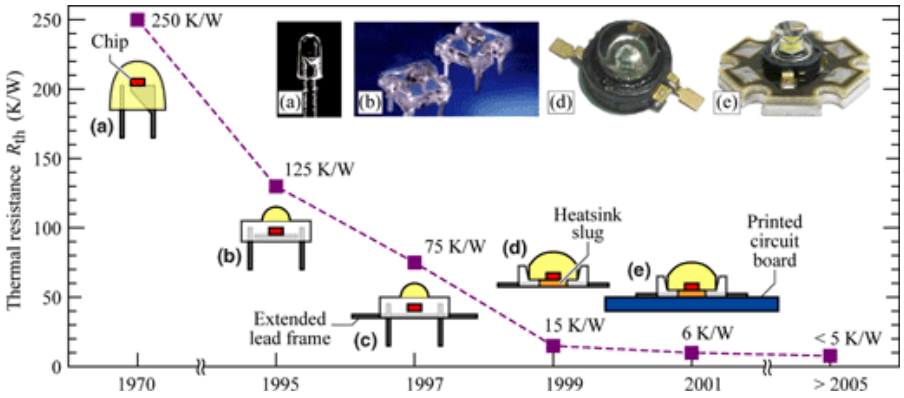

Fig. 25. Thermal resistance of LED packages: (**a**) 5 mm, (**b**) low profile, (**c**) low profile with extended lead frame, (**d**) heatsink slug, (**e**) heatsink slug mounted on PCB. Trade names for these packages are "Piranha" (**b** and **c**, Hewlett Packard Corp.), "Barracuda" (**d** and **e**, Lumileds Corp.), and "Dragon" (**d** and **e**, Osram Opto Semiconductors Corp.) (Adopted from Ref. 69).

Epoxy resins are chemically stable up to temperatures of ∼120°C. However, prolonged exposure to temperature >120°C leads to yellowing (loss of transparency).

To overcome the limited thermal stability of epoxies, ***silicone encapsulants*** have been used starting in the early 2000s. Silicone is a polymer which contains Si and O thereby resembling SiO_2 more so than epoxy resins. This resemblance suggests that silicone encapsulants are chemically and thermally stable and do not lose transparency as easily as epoxy resins. Indeed, standard silicones are stable up to temperatures of ∼160°C, ie, significantly higher than epoxy. It is desirable to develop encapsulants that are SiO_2-like because silica has excellent thermal and chemical stability (71).

Poly(methyl methacrylate) or briefly ***PMMA*** is a less common encapsulant used for LEDs. It is also known under the name of acrylic glass and under the product name Plexiglas. The relatively low refractive index of PMMA ($\bar{n} = 1.49$ in the wavelength range 500–650 nm) results in a limited extraction efficiency when used with high index semiconductors.

BIBLIOGRAPHY

"Light-Emitting Diodes and Semiconductor Lasers" in *ECT* 3rd ed., Vol. 14, pp. 269–294, by M. B. Parish, Bell Laboratories; "Light-Emitting Diodes" under "Light Generation" in *ECT* 4th ed., Vol. 15, pp. 217–246, by F. Kish, Hewlett-Packard Co.; "Light-Emitting Diodes" in *ECT* (online), posting date: December 4, 2000, by F. Kish, Hewlett-Packard Co.

1. Y.-Sh. Lin and co-workers, *Appl. Phys. Lett.* **77**, 2988 (2000).
2. T. M. Smeeton, M. J. Kappers, J. S. Barnard, M. E. Vickers, and C. J. Humphreys, *Appl. Phys. Lett.* **83**, 5419 (2003).
3. Toyoda Gosei Corporation, Japan, General LED catalogue (2000).
4. Y. Xi and E. F. Schubert, *Appl. Phys. Lett.* **85**, 2163 (2004).
5. Y. Xi and co-workers, M. H. Crawford, K. H. A. Bogart, and A. A. Allerman, *Appl. Phys. Lett.* **86**, 031907 (2005).
6. C. J. Nuese, J. J. Tietjen, J. J. Gannon, and H. F. Gossenberger, *J. Electrochem Soc.: Solid State Science* **116**, 248 (1969).
7. C. P. Kuo and co-workers, *Appl. Phys. Lett.* **57**, 2937 (1990).
8. R. M. Fletcher, C. P. Kuo, T. D. Osentowski, K. H. Huang, and M. G. Craford, *J. Elect. Mat.* **20**, 1125 (1991).
9. U.S. Pat. 5,008,718 (1991), R. M. Fletcher, C. P. Kuo, T. D. Osentowski, and V. M. Robbins.
10. H. Sugawara, M. Ishakawa, and G. Hatakoshi, *Appl. Phys. Lett.* **58**, 1010 (1991).
11. U.S. Pat. 5,153,889 (issued Oct. 6 1992), H. Sugawara and co-workers.
12. H. Sugawara, K. Itaya, H. Nozaki, and G. Hatakoshi, *Appl. Phys. Lett.* **61**, 1775 (1992).

13. E. F. Schubert, *Light-Emitting Diodes*, Cambridge University Press, New York, 2003.
14. X. Guo and E. F. Schubert, *Appl. Phys. Lett.* **78**, 3337 (2001).
15. W. B. Joyce and S. H. Wemple, *J. Appl. Phys.* **41**, 3818 (1970).
16. M. Rattier and co-workers, *IEEE J. Sel. Top. Quant. Electron.* **8**, 238 (2002).
17. X. Guo, Y. -L. Li, and E. F. Schubert, *Appl. Phys. Lett.* **79**, 1936 (2001).
18. U.S. Pat. 6,307,218 (2001), D. A. Steigerwald and co-workers, Lumileds Lighting LLC, USA.
19. LED Museum on the Internet <http://ledmuseum.home.att.net/agilent.htm> (2004).
20. D. K. Schroder, *Semiconductor material and device characterization*, John Wiley & Sons, Inc., New York, 1998.
21. K.-H. Huang and co-workers, *Appl. Phys. Lett.* **61**, 1045 (1992).
22. E. F. Schubert and co-workers, *Science* **265**, 943 (1994).
23. K. Streubel, U. Helin, V. Oskarsson, E. Backlin, and A. Johanson, *IEEE Photon. Technol. Lett.* **10**, 1685 (1998).
24. I. Schnitzer, E. Yablonovitch, C. Caneau, T. J. Gmitter, and A. Scherer, "30 % external quantum efficiency from surface-textured, thin-film light-emitting diodes," *Appl. Phys. Lett.* **63**, 2174 (1993).
25. R. Windisch and co-workers, *J. Opt. A: Pure Appl. Opt.* **1**, 512 (1999).
26. R. Windisch and co-workers, *IEEE Trans. Electron Dev.* **47**, 1492 (2000).
27. R. Windisch and co-workers, *IEEE J. Selected Topics Quant. Elect.* **8**, 248 (2002).
28. W. Schmid and co-workers, *Proc. SPIE* **3938**, 90 (2000).
29. W. Schmid and co-workers, *Proc. SPIE* **4278**, 109 (2001).
30. W. Schmid and co-workers, *IEEE J. Select. Topics Quant. Elect.* **8**, 256 (2002).
31. S. Sinzinger and J. Jahns, *Microoptics*, Wiley-VCH, New York, 1999.
32. M. R. Krames and co-workers, *Appl. Phys. Lett.* **75**, 2365 (1999).
33. J. D. Joannopoulos, R. D. Meade, and J. N. Winn, *Photonic crystals*, Princeton University Press, Princeton, 1995.
34. E. M. Purcell, *Phys. Rev.* **69**, 681 (1946).
35. F. De Martini, G. Innocenti, G. R. Jacobovitz, and P. Mataloni, *Phys. Rev. Lett.* **59**, 2955 (1987).
36. M. Suzuki, H. Yokoyama, S. D. Brorson, and E. P. Ippen, *Appl. Phys. Lett.* **58**, 998 (1991).
37. E. Yablonovitch, T. J. Gmitter, and R. Bhat, *Phys. Rev. Lett.* **61**, 2546 (1988).
38. H. Yokoyama and co-workers, *Appl. Phys. Lett.* **57**, 2814 (1990).
39. E. F. Schubert and co-workers, *Appl. Phys. Lett.* **61**, 1381 (1992).
40. N. E. J. Hunt and co-workers, in E. Burstein and C. Weisbuch, eds., *Confined electrons and photons*, Plenum Press, New York, 1995.
41. T. Nakayama, Y. Itoh, and A. Kakuta, *Appl. Phys. Lett.* **63**, 594 (1993)
42. A. Dodabalapur, L. J. Rothberg, and T. M. Miller, *Appl. Phys. Lett.* **65**, 2308 (1994).
43. G. Fabry and A. Perot, *Ann. Chim. Phys.* **16**, 115 (1899).
44. E. F. Schubert, Y. H. Wang, A. Y. Cho, L. W. Tu, and G. J. Zydzik, *Appl. Phys. Lett.* **60**, 921 (1992).
45. N. E. J. Hunt, E. F. Schubert, R. A. Logan, and G. J. Zydzik, *Appl. Phys. Lett.* **61**, 2287 (1992).
46. N. E. J. Hunt and co-workers, "High efficiency, narrow spectrum resonant cavity light-emitting diodes," in E. Burstein and C. Weisbuch, eds., *Confined electrons and photons*, Plenum Press, New York, 1995.
47. A. Yariv, *Theory and applications of quantum mechanics*, John Wiley & Sons Inc., New York, 1982, p. 143.
48. E. F. Schubert, *Doping in III-V semiconductors*, Cambridge University Press, Cambridge U.K., 1993, p. 512.
49. N. E. J. Hunt and co-workers, *Appl. Phys. Lett.* **63**, 2600 (1993).
50. K. Streubel, U. Helin, V. Oskarsson, E. Backlin, and A. Johanson, *IEEE Photon. Technol. Lett.* **10**, 1685 (1998).
51. H. A. McLeod, *Thin-Film Optical Filters*, McGraw-Hill, New York, 1989, pp. 32–43.
52. K. V. Popov, J. A. Dobrowolski, A. V. Tikhonravov, and B. T. Sullivan, *Appl. Opt.* **36**, 2139 (1997).
53. J. Xu, H. Fang, and Zh. Lin, *J. Phys D: Appl. Phys.* **34**, 445 (2001).
54. M. Ibanescu, Y. Fink, S. Fan, E. L. Thomas, J. D. Joannopoulos, *Science* **289**, 415 (2000).
55. S. D. Hart and co-workers, *Science* **296**, 510 (2002).
56. M. F. Weber, C. A. Stover, L. R. Gilbert, T. J. Nevitt, A. J. Ouderkirk, *Science* **287**, 2451 (2000).
57. Y. Fink and co-workers, *Science* **282**, 1679 (1998).
58. T. Kato and co-workers, *J. Cryst. Growth* **107**, 832 (1991).
59. S. W. Chiou, C. P. Lee, C. K. Huang, and C. W. Chen, *J. Appl. Phys.* **87**, 2052 (2000).
60. Th. Gessmann, Y. -L. Li, E. F. Schubert, J. W. Graff, J. K. Sheu, *SPIE Proceedings Series* 4996: Light Emitting Diodes: Research Manufacturing and Applications, Bellingham, WA, 2003.

61. J. K. Kim, Th. Gessmann, H. Luo, and E. F. Schubert, *Appl. Phys. Lett.* **84**, 4508 (2004).
62. M. Born and E. Wolf, *Principle of Optics*, 6th ed., Pergamon Press, New York, 1987, p. 62.
63. E. D. Palik, *Handbook of optical constants of solids*, Academic Press, Orlando, Fla., (1985) p. 357.
64. J. Q. Xi and co-workers, *Optics Letters* **30**(12) to be published (June 2005).
65. W. Thornton, Luminosity and color-rendering capability of white light, *J. Opt. Soc. Am.* **61**, 1155 (1971).
66. Y. Li, J. Shah, P. Leung, T. Gessmann, and E. F. Schubert, *Proc. SPIE* **5187**, 178 (2003).
67. M. R. Krames, Overview of current status and recent progress of LED technology, US Department of Energy Workshop "Solid State Lighting – Illuminating the Challenges" Crystal City, Va., Nov. 13–14, 2003.
68. U.S. Pat. 6,486,499 B1 (2002), M. R. Krames and co-workers.
69. M. Arik, J. Petroski, and S. Weaver, Thermal challenges in the future generation solid state lighting applications: light emitting diodes, Eighth Intersociety Conference on Thermal and Thermomechanical Phenomena in Electronic Systems (Cat. No.02CH37258) May 30–June 1 2002, p. 113, IEEE, Piscataway, N.J., 2002.
70. D. L. Barton, M. Osinski, P. Perlin, C. J. Helms, and N. H. Berg, *Proc. SPIE* **3279**, 17 (1998).
71. Crivello, V. James, personal communication.

General References

72. M. Fukuda, *Optical Semiconductor Devices*, John Wiley & Sons Inc., New York, 1999.
73. E. F. Schubert, *Light Emitting Diodes*, Cambridge University Press, Cambridge, U.K., 2003.
74. A. Žukauskas, M. S. Shur, and R. Gaska, *Introduction to Solid State Lighting*, John Wiley & Sons Inc., New York, 2002.
75. IEEE Journal on Selected Topics in Quantum Electronics, Vol. 8, No. 2, March–April 2002.

E. FRED SCHUBERT
THOMAS GESSMANN
JONG KYU KIM
Rensselaer Polytechnic Institute Troy

Related Articles

; ;